
Production and Identification of New Neutron-Rich Isotopes Close to the $N = 126$ Line at the Fragment Separator of GSI

**Produktion und Identifizierung von neuen neutronenreichen Isotopen nahe der $N = 126$ Linie
am Fragmentseparator der GSI**

Zur Erlangung des Grades eines Doktors der Naturwissenschaften (Dr. rer. nat.)
Genehmigte Dissertation im Fachbereich Physik von Heidi Ayse Rösch-Kabadayi
Tag der Einreichung: June 24, 2025, Tag der Prüfung: July 21, 2025

1. Gutachten: Prof. Dr. Joachim Enders
2. Gutachten: Prof. Dr. Christoph Scheidenberger
Darmstadt, Technische Universität Darmstadt



TECHNISCHE
UNIVERSITÄT
DARMSTADT

Physics Department
Institut für Kernphysik
AG Enders

Production and Identification of New Neutron-Rich Isotopes Close to the $N = 126$ Line at the Fragment Separator of GSI

Produktion und Identifizierung von neuen neutronenreichen Isotopen nahe der $N = 126$ Linie am Fragmentseparator der GSI

Accepted doctoral thesis in the department of Physics by Heidi Ayse Rösch-Kabadayi

Date of submission: June 24, 2025

Date of thesis defense: July 21, 2025

Darmstadt, Technische Universität Darmstadt

Bitte zitieren Sie dieses Dokument als:

URN: urn:nbn:de:tuda-tuprints-314067

DOI: <https://doi.org/10.26083/tuprints-00031406>

Jahr der Veröffentlichung auf TUprints: 2025

Dieses Dokument wird bereitgestellt von tuprints,

E-Publishing-Service der TU Darmstadt

<https://tuprints.ulb.tu-darmstadt.de>

tuprints@ulb.tu-darmstadt.de

Die Veröffentlichung steht unter folgender Creative Commons Lizenz:

Namensnennung 4.0 International

<https://creativecommons.org/licenses/by/4.0/>

This work is licensed under a Creative Commons License:

Attribution 4.0 International

<https://creativecommons.org/licenses/by/4.0/>

To a little creature who has no name yet.

Erklärungen laut Promotionsordnung

§ 8 Abs. 1 lit. d PromO

Ich versichere hiermit, dass zu einem vorherigen Zeitpunkt noch keine Promotion versucht wurde. In diesem Fall sind nähere Angaben über Zeitpunkt, Hochschule, Dissertationsthema und Ergebnis dieses Versuchs mitzuteilen.

§ 9 Abs. 1 PromO

Ich versichere hiermit, dass die vorliegende Dissertation – abgesehen von den in ihr ausdrücklich genannten Hilfen – selbstständig verfasst wurde und dass die „Grundsätze zur Sicherung guter wissenschaftlicher Praxis an der Technischen Universität Darmstadt“ und die „Leitlinien zum Umgang mit digitalen Forschungsdaten an der TU Darmstadt“ in den jeweils aktuellen Versionen bei der Verfassung der Dissertation beachtet wurden.

§ 9 Abs. 2 PromO

Die Arbeit hat bisher noch nicht zu Prüfungszwecken gedient.

Darmstadt, June 24, 2025

Heidi Ayse Rösch-Kabadayi

Acknowledgments

This work is the result of the many forms of support and encouragement I have received throughout this journey. I am sincerely grateful to all who, in their own way, helped me arrive at this moment.

First of all I would like to express my sincere gratitude to Prof. Joachim Enders, who has been a constant source of support and guidance since the beginning of my physics studies. He was always available whenever I needed advice or feedback, and closely followed the progress of this analysis, providing valuable input at every stage. His expertise and commitment were instrumental in shaping the outcome of this work.

I am very grateful to Dr. Stéphane Pietri, the spokesperson of the S468 experiment, for entrusting me with the data and for the continuous support throughout the analysis. He closely followed each step of the process and provided expert guidance that was essential for navigating the challenges of this work.

I would especially like to thank Prof. Teresa Kurtukian Nieto, whose unwavering support and motivation were invaluable throughout this project. Beyond her expert knowledge and guidance throughout the analysis, her encouragement and positive spirit helped me push through challenging phases of the analysis. This work would not have been completed without her.

I am thankful to Prof. Tuomas Grahn, Prof. Alison Bruce, Dr. Jan-Paul Hucka, and Dr. Minna Luoma for the fruitful collaboration, which greatly contributed to the progress of this work.

The S468 experiment would not have been possible without the members of the FRS and Super-FRS working groups, the participants of the S468 experiment and the Super-FRS Experimental Collaboration.

Finally, I would like to thank my family and friends. Without Dr. İnci Rösch and Dr. Wilfried Rösch—my parents and lifelong role models—none of this would have been

possible. I drew strength and perseverance from Erdem Kabadayi, whose unwavering support meant the world to me. My brothers, Peter Hilmi Rösch and Dr. Karl Ömer Rösch, together with their families, have always been a source of joy and energy. Erdem Kabadayi, Peter Hilmi Rösch and Dr. Jan Wissmann were my last second support and crisis management team.

This work was supported by the GSI-TU Darmstadt Cooperation Contract and the BMBF Project No. 05P21RDFN1. Additional funding was provided through the HFHF program, funded by the Hessian Ministry of Science and the Arts (HMWK) and the Helmholtz Association.

Abstract

This thesis presents the data analysis and particle identification of the S468 experiment performed at the Fragment Separator (FRS) of GSI. The experiment targeted the neutron-rich region near the $N = 126$ shell closure, a key area for understanding the astrophysical r -process but largely unexplored due to the experimental challenges in producing such exotic nuclei. Within this work, five new isotopes were identified for the first time: ^{184}Tm , ^{195}Ta , ^{198}W , ^{200}Re , and ^{201}Re —the latter located directly on the $N = 126$ line. These discoveries extend the known nuclear chart and highlight the capabilities of the FRS in accessing this region. In addition, the dataset offers promising potential for determining unknown β -decay half-lives and production cross sections, contributing valuable input for both nuclear structure studies and nucleosynthesis modeling.

Zusammenfassung

In dieser Arbeit wird die Datenanalyse und Teilchenidentifikation des S468-Experiments, das am Fragmentseparator (FRS) der GSI durchgeführt wurde präsentiert. Ziel des Experiments war die Untersuchung des neutronenreichen Bereichs nahe der magischen Neutronenzahl $N = 126$, einem wichtigen Bereich für das Verständnis des astrophysikalischen r -Prozesses. Aufgrund experimenteller Herausforderungen ist dieser Bereich bislang weitgehend unerforscht. Im Rahmen dieser Arbeit konnten fünf neue Isotope erstmals identifiziert werden: ^{184}Tm , ^{195}Ta , ^{198}W , ^{200}Re und ^{201}Re – letzteres befindet sich direkt auf der $N = 126$ -Linie. Diese Entdeckungen erweitern die bekannte Nuklidkarte und unterstreichen die Leistungsfähigkeit des FRS beim Zugang zu diesem Gebiet. Darüber hinaus bietet der Datensatz vielversprechendes Potenzial zur Bestimmung bislang unbekannter β -Zerfallshalbwertszeiten und Produktionsquerschnitte und liefert damit wertvolle Beiträge sowohl für kernphysikalische Strukturstudien als auch für die Modellierung der Nukleosynthese.

Contents

Acknowledgments	vii
1 Introduction	1
2 Nucleosynthesis and the r-Process	5
2.1 Solar Abundances and Nucleosynthesis Processes	5
2.2 The r-Process	8
2.3 Waiting Points Along the r-Process Path	8
2.4 Challenges and the Need for Experimental Data	10
3 Production of Heavy Neutron-Rich Isotopes	13
3.1 Production Mechanisms	13
3.2 Rare Ion Beam Facilities	16
3.3 The Accelerator Facility of GSI	17
3.4 The GSI Fragments Separator FRS	18
3.5 FAIR's Super FRS and FAIR Phase 0	21
4 The Experiment Search For New Isotopes	25
4.1 Scope of the Experiment S468	25
4.2 Experimental Setup	26
5 Data Analysis	29
5.1 Identification of the Charge Z	29
5.2 Identification of the Mass over Charge Ratio AoQ	39
5.3 Gates for Background Reduction	45
5.4 Assignment and Counting of the Identified Isotopes	47
6 Results and Discussion	53
6.1 Production and Identification in the Au Setting	53

6.2	Production and Identification in the W Setting	56
6.3	Production and Identification in the Ta Setting	58
6.4	Production and Identification in the Lu Setting	61
6.5	New Isotopes	63
7	Perspectives for Continued Research on the S468 Data	69
7.1	Cross Section of Nuclei Close to $N = 126$	69
7.2	Beta-decay of Nuclei Close to $N = 126$	71
8	Conclusion	73

1 Introduction

In the past 130 years, a series of foundational discoveries has profoundly shaped our understanding of the composition, structure, and origin of matter.

The discovery of radioactivity in 1896 by Becquerel [1] motivated decay studies and led to the discovery of isotopes from naturally occurring decay chains. The atomic model composed of a positively charged massive nucleus in the core was established in 1911 by Rutherford [2]. After observing that hydrogen nuclei were ejected from nitrogen atoms when bombarded with α -particles, he suggested the nucleus of the hydrogen atom as a fundamental building block for other nuclei. Thus, the proton was discovered in 1919 [3]. In order to explain the mass of nuclei without adding charge, Rutherford postulated the existence of an additional fundamental building block of the nucleus with neutral charge and a mass similar to the proton in 1920. The neutron was discovered in 1932 by Chadwick [4].

These groundbreaking discoveries enabled the classification of isotopes based on their number of nucleons and offered crucial insights into nuclear reactions and transmutations. They advanced the understanding of the creation of atomic nuclei and contributed to addressing the fundamental question of the origin of matter. The process by which elements are formed through nuclear reactions is called nucleosynthesis. The first idea of stellar nucleosynthesis suggesting nuclear fusion as an explanation for the energy radiated by stars originates from Eddington's paper published already in 1920 [5]. The first concrete theory of stellar formation that modeled hydrogen fusion into helium in stars was established by Bethe and Weizsäcker in 1938 when they formulated the proton-proton chain and the CNO cycle [6]. Building on decades of astronomical observations and experimental data, the full theory of stellar nucleosynthesis appeared in 1957. In the paper "Synthesis of the Elements in Stars" Burbidge, Burbidge, Fowler, and Hoyle explained how nearly all elements are formed by nuclear reactions in stars [7]. They systematically argued that all elements heavier than helium are synthesized through nuclear processes in stars. Furthermore, they offered explanations for the abundances

observed in the universe attributing them to different nuclear processes occurring in stars throughout their life-cycles. These processes included hydrogen and helium burning, carbon and oxygen fusion, and neutron-capture mechanisms such as the s-process (slow neutron capture) and r-process (rapid neutron capture), as well as proton-capture and explosive nucleosynthesis.

While connecting patterns observed in the solar system abundances with different nuclear processes and hence establishing the foundations of nuclear astrophysics, they left several critical questions –particularly concerning the r-process– unresolved. The rapid neutron capture mechanism is crucial to explain the existence of neutron-rich nuclei beyond iron especially near the abundance peaks at $A \sim 130$ and $A \sim 195$, but the astronomical site or event providing the extreme neutron flux required by the process to take place remained unknown. Also theoretical simulations relying heavily on nuclear properties of the isotopes along the r-process path were lacking experimental data, due to the inaccessibility of these isotopes far from stability.

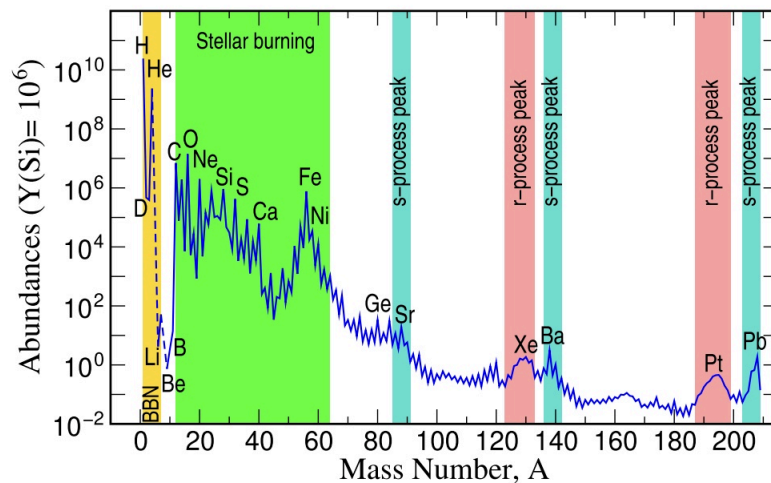


Figure 1.1: Relative abundances of isotopes Y in function of their mass numbers A, scaled to an abundance of 10^6 for Si. The abundances are deduced from element ratios in solar spectra and isotopic ratios from meteorites and terrestrial values [8] and [9]. Figure from [10].

These fundamentally important questions have motivated significant advances in observational astronomy, nuclear theory, and experimental capabilities. Details of the current

status of the r-process nucleosynthesis can be found in [10] and in [11]. The detection of neutron star mergers, particularly the 2017 event GW170817, provided the first direct evidence that such collisions can serve as r-process sites [12]. This event marked a breakthrough in multi-messenger astronomy, as it was observed through a combination of gravitational waves, electromagnetic radiation (from gamma rays to optical and X-rays), and neutrinos, all tracing back to a single astrophysical source [13]. Such simultaneous detection allows for a more comprehensive understanding of the physical processes involved in these extreme environments.

Nonetheless, key challenges persist. Despite the improvements made in the experimental methods to produce, identify and investigate rare neutron-rich isotopes, a major limitation in r-process modeling still lies in the lack of experimental data for the neutron-rich nuclei involved. This is especially true for the region around the neutron magic number $N = 126$, which corresponds to the third r-process abundance peak near mass number $A \sim 195$. Nuclei at $N = 126$ have closed neutron shells and serve as critical waiting points during the r-process. This slows down the production of isotopes in this region and influences the final abundance pattern. Yet, very few isotopes in this region have been observed experimentally due to experimental challenges.

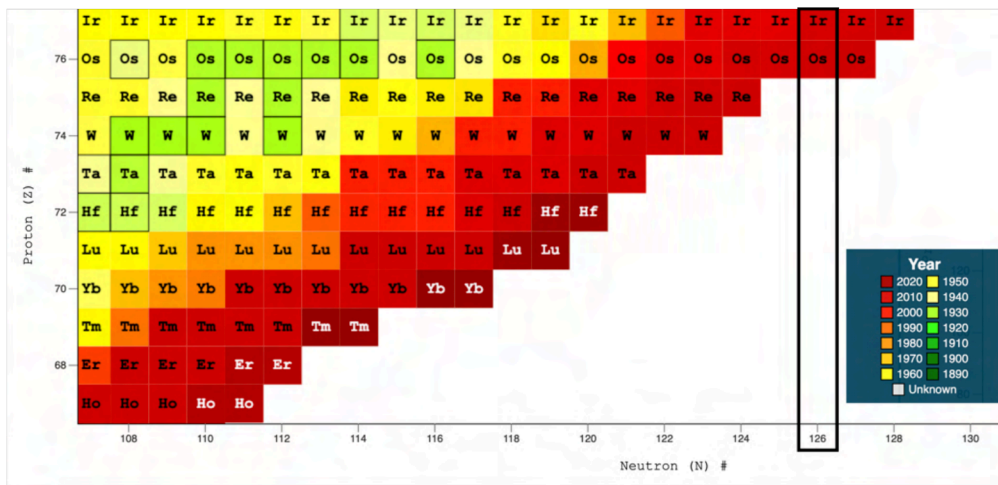


Figure 1.2: Nuclear chart in the region of $N = 126$. The isotopes are color-coded according to their date of discovery [14].

To address this gap, an experiment was conducted at the GSI Fragment Separator (FRS) in 2020 as part of FAIR Phase 0. During this campaign, the existing facility was operated

using newly developed FAIR equipment, following modernization upgrades to prepare for the requirements of the next-generation FAIR facility currently under construction. The S468 experiment produced isotopes near $N = 126$ in order to identify and study the nuclear properties of isotopes in this exotic region, at the edge of the known isotopes. In addition to the identification of new isotopes, the experiment was aimed at measuring nuclear properties such as masses, cross sections, and beta-decay lifetimes in a single experimental setup.

In this thesis, data analysis for the identification of isotopes produced in the S468 experiment will be presented. New isotopes, including the $N = 126$ isotope ^{201}Re will be presented.

The following two chapters (Chapters 2 and 3) will introduce how neutron-rich isotopes are generated in nature through nucleosynthesis, focusing on the rapid neutron capture process, and how they can be produced in facilities, such as in the GSI fragment separator, respectively. In chapter 4 the scope and experimental setup of the S468 will be described. The detailed description of the data analysis leading to the identification of the produced isotopes can be found in Chapter 5, while the results of the analysis and a discussion will follow in chapter 6. In chapter 7 the further analysis of the data in order to measure properties such as beta decay lifetimes and cross sections will be motivated. In the last chapter, the results will be summarized and an outlook will be given.

2 Nucleosynthesis and the r-Process

The origin of matter is one of the most fundamental questions in science. Researchers across disciplines—including nuclear physics and astrophysics—are working to piece together the story of how the elements in the universe were formed. Today, it is well established that all nuclei heavier than lithium are synthesized in stars or stellar explosions. Yet, many open questions remain, particularly concerning the rapid neutron capture process, which is responsible for creating about half of the elements heavier than iron.

This chapter outlines how we know what we know about nucleosynthesis, starting with the interpretation of patterns in the solar abundances that reflect the contributions of different nuclear processes. The r-process will then be discussed in detail. Next, the concept of waiting points in the r-process path that lead to the formation of abundance peaks will be explained. Finally, current uncertainties will be addressed, with a focus on how measuring the properties of nuclei near $N = 126$ can help advance the understanding of the r-process.

2.1 Solar Abundances and Nucleosynthesis Processes

Solar abundances are mainly determined via spectroscopic observations of the Sun and through analysis of primitive meteorites. Both methods result in similar element abundances. The isotopic abundances are then derived from terrestrial ratios. While the solar abundances are broadly representative of many neighboring stars with an age similar to that of the sun, older stars abundances can show significant deviations, in particular for elements formed by neutron capture processes. The similarity of abundances in stars with similar age indicates common initial conditions at formation. In contrast the deviations in older stars reflect chemical conditions from earlier galactic stages.

In the following figure (Figure 2.1) solar abundances of isotopes as a function of their mass numbers are plotted. For multiple isobars with the same mass number the sum of the isobar abundances is shown.

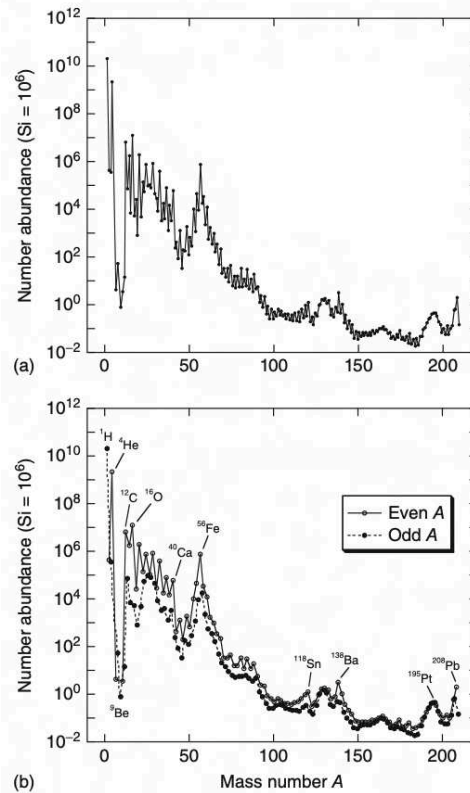


Figure 2.1: a) Relative abundances of isotopes in function of their mass numbers A , scaled for an abundance of 10^6 Si nuclides. The abundances are deduced from element ratios in solar spectra and isotopic ratios from meteorites and terrestrial values. b) Abundance curves of odd and even- A nuclides. Data from [8] and figure from [15]

The vast majority of the solar mass consists of ^1H with 71.2% and ^4He with 27.4%. There is a minimum in the abundance curve for $A = 5 - 11$ —related to low abundances of Li, Be and B elements. The combined abundances of ^{12}C and ^{16}O contribute 1.5% to the total solar abundance. Overall the abundance of elements decreases with increasing mass number, yet notable peaks occur. The first distinct peak at $A = 50 - 65$ is described as

the iron peak, followed by double-peaks at $A = 110 - 150$ and $A = 180 - 210$ attributed to neutron capture processes. In addition, an enhanced abundance of even- A nuclides compared to odd- A nuclides is observed. This characteristic shape of the abundance curve reveals properties of the nuclei and the nucleosynthetic processes that occurred.

In general terms, the origins of elements can be divided into various nucleosynthesis processes, each predominantly responsible for the production specific groups of nuclides and characteristic features in the observed abundance pattern. A detailed and comprehensive overview of all nucleosynthesis processes can be found in [15]. The most relevant processes are briefly summarized below.

- **Big Bang Nucleosynthesis (BBN):** Responsible for the formation of the lightest elements—hydrogen, helium, and small amounts of lithium and deuterium—during the first few minutes after the Big Bang [16].
- **Stellar Nucleosynthesis:** Occurs throughout the life cycles of stars. Stable stars maintain an equilibrium between gravitational and internal forces from nuclear reactions. As the star contracts under gravity the temperature rises until the Coulomb barrier of a certain nuclide is overcome and its fusion is enabled. Fusion in stellar cores builds up elements from hydrogen to iron through successive burning stages (H, He, C, Ne, O, Si). Starting with the nuclei that have the lowest Coulomb barrier. Once they are consumed, the star contracts until the temperature to overcome the next lowest Coulomb barrier is reached.

Fusion reactions beyond iron do not release energy. Elements heavier than iron must be formed through different mechanisms, such as neutron capture.

- **s-Process (slow neutron capture):** Occurs in asymptotic giant branch (AGB) stars, where the intershell region between the H- and He-burning shell contains the ingredients for the production of free neutrons. The neutron sources—mainly ^{13}C and ^{22}Ne —are mixed with seed nuclei (e.g. iron) through thermal impulses. This initiates the s-process, enabling the step-by-step build-up of heavy elements through neutron capture. The neutron flux is low enough so that beta decays typically occur before additional neutrons are captured. This process forms stable isotopes along the valley of beta stability and accounts for many of the isotopes observed around $A \approx 90-210$ [17].
- **r-Process (rapid neutron capture):** Requires extremely high neutron fluxes, such that neutron capture occurs faster than beta decay. This drives the creation of very neutron-rich isotopes far from stability and accounts for roughly half of the heavy

elements beyond iron. The r-process will be described in more detail in the following section (Section 2.2).

- **Other processes:** Include the *p-process* (photodisintegration or proton capture), the *ν -process* (neutrino-induced nucleosynthesis), *vp-process* and explosive nucleosynthesis in supernovae and neutron star mergers.

2.2 The r-Process

In environments with extremely high neutron densities—typically above 10^{20}cm^{-3} —neutron capture rates are so rapid that nuclei do not have sufficient time to undergo beta decay before capturing additional neutrons. As a result, very neutron-rich isotopes far from stability are created. As the free neutrons are rapidly consumed during the r-process, the neutron flux decreases and the isotopes undergo successive beta decays towards stability. The r-process thus follows a path far from the stability valley, producing highly neutron-rich isotopes. The final abundance pattern is determined by the dynamic balance of neutron capture processes, beta-decay timescales and—in case of super-heavy isotopes beyond $A = 280$ —fission recycling.

For decades, the astrophysical site of the r-process remained uncertain. While core-collapse supernovae were early candidates, simulations struggled to reproduce the necessary conditions. The breakthrough came with the multi-messenger observation of the neutron star merger GW170817, whose counterpart (a kilonova) showed spectral signatures consistent with r-process nucleosynthesis [12]. This confirmed that such mergers are a dominant site for the r-process.

The solar r-process abundances are derived by subtracting the s-process component—well reproduced using the classical s-process model [18]—from the total abundances. Figure 2.2 shows the resulting abundances for $A > 90$. The characteristic peaks at $A = 130$ and $A = 195$ are formed by nuclei accumulating at the neutron magic numbers, that act as major waiting points during the r-process (Section 2.3).

2.3 Waiting Points Along the r-Process Path

The r-process path extends through extremely neutron-rich regions of the nuclear chart, far from the valley of stability. As seed nuclei rapidly capture neutrons, the process proceeds

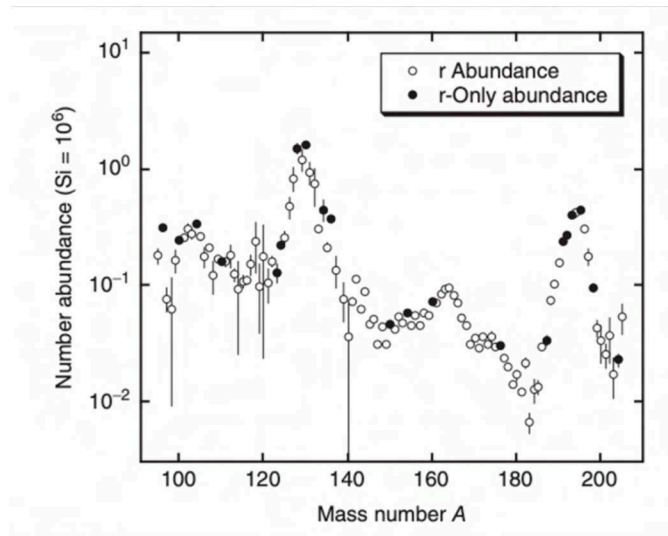


Figure 2.2: Solar r-process abundances for $A > 90$. The r-process contributions are derived from the total solar abundances by subtracting the s-process component, that can be calculated using the classical s-process model [18]. The nuclides that are created exclusively by the r-process are shown as full circles. Figure from [15]

through chains of isotopes with increasingly higher neutron numbers. However, at certain points, the progression of the r-process decelerates significantly due to reduced neutron capture probabilities and long beta-decay-lifetimes. This can occur, for instance, when an equilibrium is reached between the neutron capture and its inverse, the photodisintegration, reaction. At this moment the nuclei have to undergo beta-decay before they can continue the neutron capture process. Because beta-decay-timescales during the r-process are longer than neutron capture rates, the nuclei accumulate at these so called waiting points. Major waiting points are formed at neutron shell closure occurring at the magic numbers, $N = 50, 82, 126, \dots$. For these nuclei the neutron capture cross sections are low and they are slightly more stable with longer beta-decay-lifetimes. When they are reached, the r-process is stalled significantly and nuclei accumulate.

Waiting points in the r-process arise from the interplay of several nuclear properties that influence r-process path. Besides the most prominent nuclei with closed neutron shells at magic numbers, even- N nuclei tend to have longer beta-decay half-lives compared to their

odd-N neighbors due to pairing effects. This reinforces their role as local waiting points. In regions with less well-understood nuclear structure, especially far from stability, other nuclear factors may also create secondary waiting points. Nuclear deformations in these regions can affect the beta-lifetimes, the level density or neutron separation energy and even the magic numbers, creating unexpected waiting points. The effects of these factors are model-dependent and require experimental validation.

Figure 2.3 shows the building blocks of the r-process path. As the neutron densities decrease, neutron capture rates drop and beta-decay becomes the dominant mechanism. Nucleosynthesis continues through the waiting points, as they undergo beta decays along isobaric chains until the first long lived or stable isotope is reached. The solar abundance peaks arise because of the significant accumulation at the magic neutron numbers at the end of the neutron flux when the beta-decays begin.

The concept of waiting points helps explain why r-process nucleosynthesis leads to a non-uniform distribution of heavy element abundances. However, the exact behavior of these waiting points depends on nuclear properties that are often not known experimentally, especially in the neutron-rich regions relevant to the r-process.

2.4 Challenges and the Need for Experimental Data

A critical first step in addressing the open questions of the r-process is the production and identification of the relevant neutron-rich nuclei. This allows for the determination of which isotopes can be accessed at existing and planned accelerator facilities, and under what conditions. Mapping the production capabilities at different facilities helps guide both theoretical efforts and experimental priorities in targeting nuclei near waiting points and shell closures.

Many key aspects of the r-process remain poorly constrained due to the lack of experimental data. The majority of the nuclei along the r-process path are extremely neutron-rich and short-lived, making them difficult to produce and study in the laboratory.

Uncertainties remain in:

- **Nuclear masses**, which determine the energetics of neutron capture, beta-decay and photo-disintegration rates.
- **Beta-decay half-lives**, which influence the timescale of material flow and shape the light curves in kilonova events.

-
- **Neutron capture cross sections**, which shape the r-process path.
 - **Fission properties**, which are critical at the heaviest mass numbers and influence the light curves in kilonova events.
 - **Production cross sections**, which determine the experimental accessibility of neutron-rich isotopes and constrain the initial population of nuclei in r-process nucleosynthesis models.

Improved experimental access to r-process nuclei, particularly near the $N = 126$ shell closure, is essential for reducing model uncertainties. Measuring these nuclear properties allows for more accurate reaction network calculations and more reliable predictions of abundance patterns.

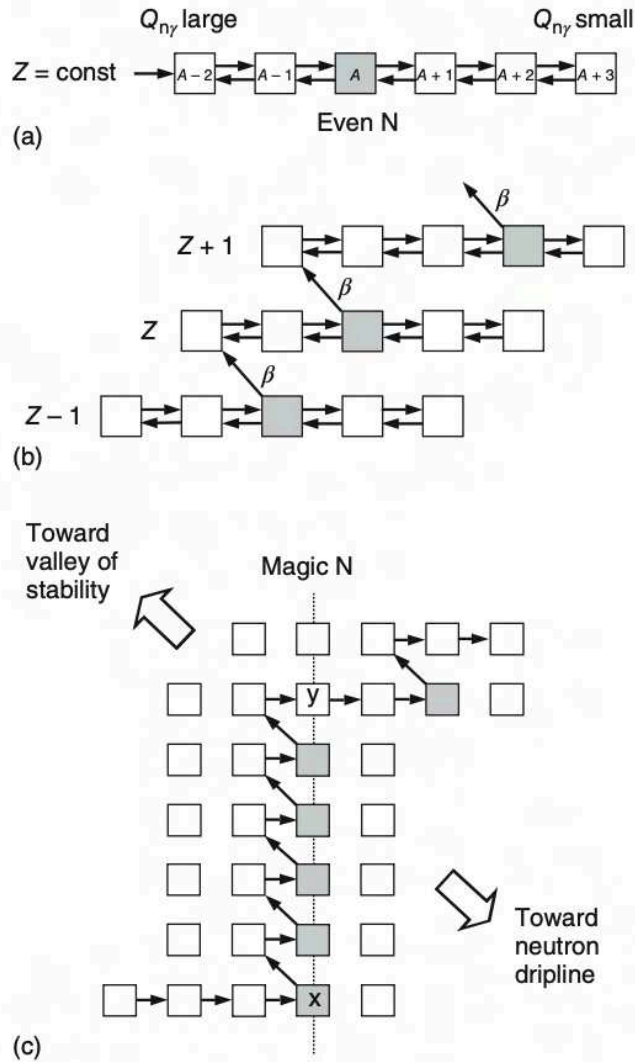


Figure 2.3: Basic segments of the r-Process path [18]. Shaded squares mark the waiting points. a) Isotopic chain in the neutron capture photodisintegration equilibrium. b) Transfer to the next isotopic chain from the waiting point through beta-decay. c) The r-process path at neutron magic numbers.

3 Production of Heavy Neutron-Rich Isotopes

Heavy neutron-rich nuclei far from stability have short life times and cannot be naturally observed. They must be produced in a laboratory and identified before their properties can be investigated. The nuclear reactions that can induce the production of Rare Isotope Beams (RIB) require extreme conditions that are reproduced in accelerator facilities.

In this chapter, the different production mechanisms and accelerator facilities that enable the artificial production of these rare exotic isotopes will be described. In particular, the basic structure of the projectile Fragment Separator (FRS, [19]) of the GSI Helmholtzzentrum für Schwerionenforschung, Darmstadt (Germany) will be introduced.

3.1 Production Mechanisms

Nuclear reactions induced by a projectile that impinges on a target can lead to the production of rare isotopes. The choice of the projectile, target, and nuclear reaction to be used as a production mechanism depends on the isotope of interest and the properties required, including intensity and energy.

Each reaction produces a whole variety of different isotopes. The production rate of the isotope of interest compared to other isotopes created by the reaction depends on the relative production cross section. For the most exotic isotopes the production cross sections are expected to be low, which means that efficient separation techniques are needed to extract identify and investigate the isotope in question.

There are two main options of separation. The isotopes can be produced directly in the form of energetic radioactive ion beams and separated in flight, a technique known as "in-flight separation", or they can be produced at rest and then accelerated subsequently, the "isotope separation on-line" (ISOL) technique. The ISOL technique produces radioactive ion beams by bombarding a thick target with high-energy protons or light ions. The

reaction products diffuse out of the hot target material, are ionized, and then extracted, mass-separated, and delivered to experiments. However, it is not suitable for producing heavy neutron-rich nuclei near the $N = 126$ shell closure, because many of these are refractory elements that bind strongly to the target and are difficult to release [20]. In addition, their typically short half-lives mean they often decay before they can be extracted and identified.

Figure 3.1 summarizes features of the main nuclear reaction used to produce RIBs, such as the energies of the products, their production rates, and the production area in the nuclear chart relative to the projectile and target used. The nuclear reactions used to

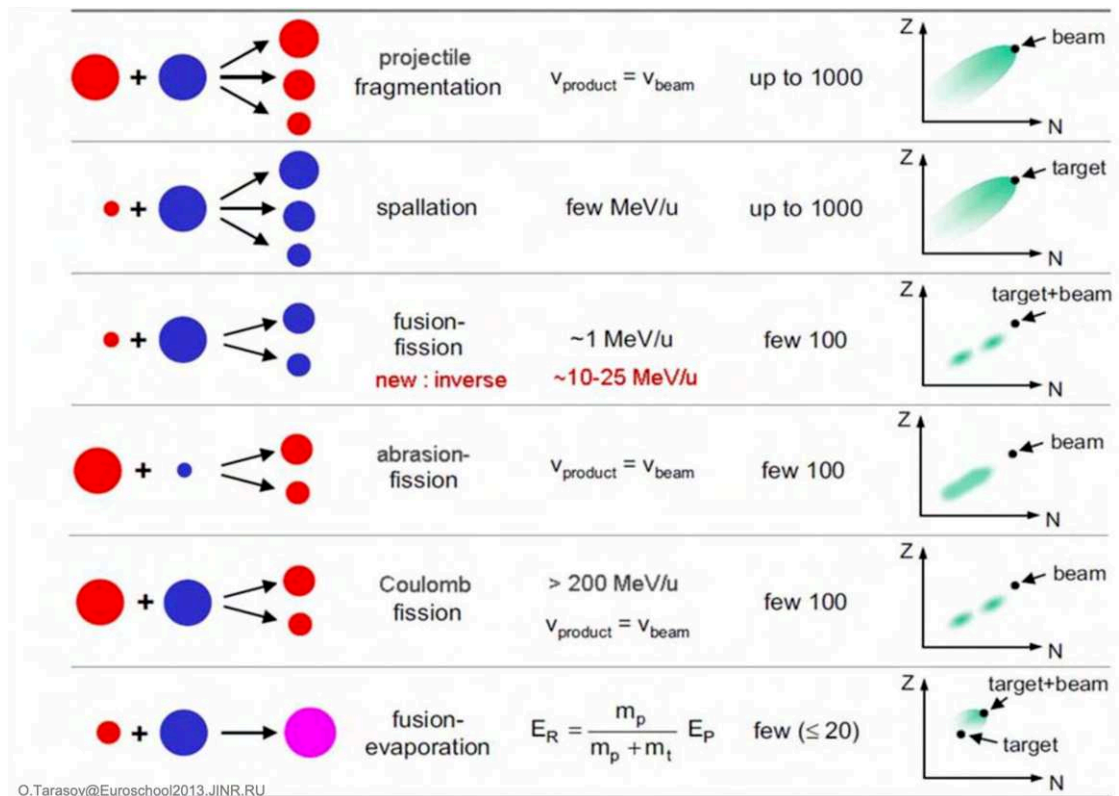


Figure 3.1: Schematic representation of the main production mechanisms for rare isotope beams [21]. Projectile and projectile fragments are represented by red circles, whereas blue circles are target/ target fragments.

create RIBs with the in-flight separation technique are essential for this thesis. After

projectile fragmentation and fission reactions, the velocity of the products is the beam velocity, and the produced isotopes can be separated in flight.

Projectile Fragmentation:

Projectile fragmentation occurs when nuclei in a primary ion beam collide with target nuclei, causing the projectile to break into smaller fragments and eject nucleons, primarily neutrons, due to the energy released. As a result, the projectile fragments are lighter than the original projectile. In heavy nuclei, neutrons are more likely to evaporate, which influences the fragment distribution. Hence, the production of neutron-rich isotopes from projectile fragmentation of a fast heavy beam remains challenging. However, the removal of several neutrons is possible and typically referred as "cold fragmentation". [22].

The secondary beam, composed of these projectile fragments, generally continues in the same direction as the original beam with similar energy. Consequently, the quality of separation and identification of the fragments heavily depends on the primary beam's properties. These initial conditions — such as emittance, momentum spread, and solid angle—determined during production, directly influence the efficiency of the separator, which is limited by its acceptance.

In projectile fragmentation, lighter nuclei are produced by removing nucleons from the projectile. As more nucleons are removed, the momentum spread of the fragments increases, especially for nuclei much lighter than the original projectile [23, 24]. Production rates tend to decrease for lighter nuclei and for those with neutron-to-proton ratios diverging from that of the projectile. This distribution is often represented as a diagonal region in the nuclear chart, roughly extending toward the "southwest" from the original projectile's position (Fig. 3.1).

Fission

Fission is used to produce neutron-rich isotopes. In projectile fission, high-energy heavy projectiles — such as uranium — are excited through interactions with the target nuclei, causing them to split into smaller nuclei (fission fragments), neutrons, and energy. Due to the neutron excess, the resulting fission fragments are typically more neutron-rich than the original projectile. After fission, the fragments have a wide momentum spread and are emitted in all directions, covering the entire solid angle. This wide distribution in the rest frame of the fissioning nucleus can significantly reduce the efficiency of fragment separation. Fission fragments represent a secondary and often undesired background

in experiments aimed at producing heavy neutron-rich nuclei. They are typically lighter than the nuclei of interest and can be produced simultaneously with projectile fragments—especially when using heavy projectiles. Due to their kinematics, some fission fragments can also be transmitted through the separator, potentially contaminating the desired signal.

3.2 Rare Ion Beam Facilities

While pioneering facilities such as ISOLDE at CERN have been operational since the 1960s, primarily for beta-decay studies without post- of radioactive ion beams for nuclear physics research were constructed in the 1990s at several locations [25]. Facilities based on the in-flight separation technique using mainly projectile fragmentation were built, for instance, at GANIL in France [26], RIKEN in Japan [27], MSU in USA [28], GSI in Germany [19] or IMP in China [29]. Examples for facilities using the isotope separation online, ISOL-technique include Spiral and Alto in France [30, 31], ISAC in Canada [32] and REX ISOLDE in Switzerland/France [33].

The success of these first-generation RIB facilities contributes significantly to the understanding of nuclear structure. For example experiments at these facilities enabled detailed studies of exotic phenomena such as the halo structure in ^{11}Li and ^6He [34], the breakdown of traditional magic numbers in the island of inversion near ^{32}Mg [35], and the evolution of shell structure in neutron-rich nuclei like ^{24}O and ^{42}Si [36, 37]. However, short half-lives and small production cross sections complicate the detection, identification and investigation of the nuclei the further they are from stability. This motivated the construction of next-generation separators with enhanced performances in the production of exotic nuclei.

The projectile fragmentation-based next generation facilities that are already in operation are RIBF (Japan, [38]) and FRIB (US, [39]). The Super-FRS at FAIR (Germany, [40]) is currently under construction and is expected to become fully operational in the coming years. However, commissioning activities began during the FAIR Phase 0 stage, involving preparatory work, component testing, and early commissioning efforts using the existing GSI facility in combination with FAIR equipment. Super-FRS and FAIR Phase 0 will be described in more detail in Section 3.5.

3.3 The Accelerator Facility of GSI

Darmstadt's accelerator facility GSI Helmholtzzentrum für Schwerionenforschung in Germany is a leading center for heavy ion research. GSI has the capacity to accelerate every naturally existing ion to velocities up to 90% of light velocity. The research conducted at GSI spans multiple fields, including particle physics, nuclear physics, atomic physics, plasma physics, bio-physics, material science, and tumor therapy. A schematic diagram of the facility is presented Figure 3.2.

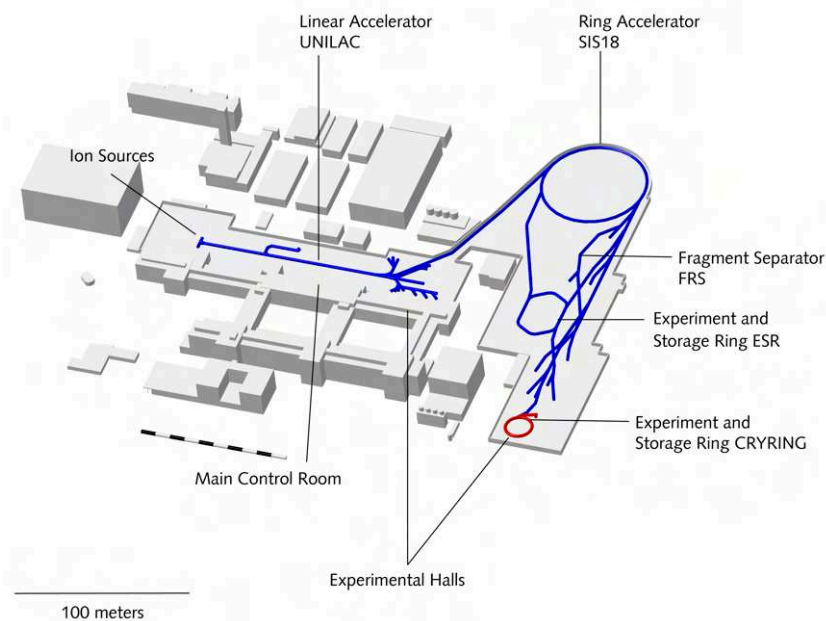


Figure 3.2: Schematic illustration of GSI Helmholtzzentrum für Schwerionenforschung [41].

The facility primarily comprises six components, which are essential for supplying all the different experiments with an ion beam tailored to their particular needs.

Beam production begins at the ion source [42], where the desired ions are created by ionizing neutral atoms or molecules, resulting in positively charged ions. These ions are then extracted and initially accelerated using electric fields.

Commissioned in 1975, the Universal Linear Accelerator (UNILAC, [43, 44]) was the first accelerator built at GSI. The ions extracted from the ion source are further accelerated in UNILAC to velocities of up to 0.2 times the speed of light.

From there, the beams can either be directed to experimental halls for research or injected into the SIS18 synchrotron [45, 46, 47], which was added in 1990. With each revolution in the 216-meter-circumference ring, the ions are incrementally accelerated to higher velocities. The maximum speed achievable in the SIS18 synchrotron is approximately 90% of the speed of light.

After reaching the desired velocity in the SIS18 synchrotron, the ions can either be transferred to the Experimental Storage Ring (ESR, [45, 48]) for further experimentation or directed to an experiment hall. Additionally, the high-energy primary beam from SIS18 can be used to generate secondary beams of rare, radioactive isotopes in the FRS [19], where the projectile fragments are identified. The specific isotopes of interest are isolated and delivered to experiments for further study.

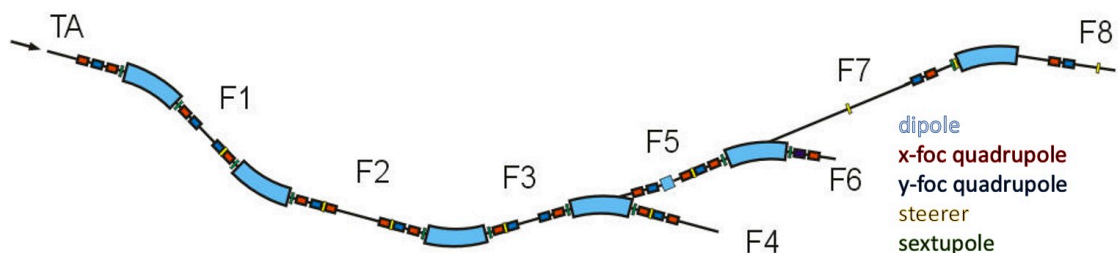


Figure 3.3: A schematic illustration of the FRS beam line starting from the target (TA). The magnets and focal planes (F1-F8) are indicated [49]. The FRS directs the beam either to the final focal plane F4, as in the experiment described in Chapter 4, to the ESR via F6 or to the final focal plane F8 for experiments.

3.4 The GSI Fragments Separator FRS

The Projectile Fragment Separator (FRS, [19]) enables the production, identification, selection, and separation of the desired isotope from other fragments. Providing a radioactive ion beam for experimental use involves three essential tasks: generating radioactive isotopes, isolating the desired ion beam, and identifying the isotopes produced.

Production and Separation:

In the FRS, exotic isotopes are generated when the primary beam from GSI's accelerator ring SIS18 strikes a production target positioned at the entrance of the separator. This target is mounted on a target station capable of holding up to 75 different targets. Isotope production occurs at FRS energies and conditions primarily via two mechanisms: fragmentation or fission. Regardless of the method, the isotope of interest is created alongside numerous other reaction products. Before it can be used in experiments, the isotope must be separated from these unwanted fragments and shaped into a beam that meets specific experimental requirements.

In the FRS, isotopes are separated during their flight through the system. The primary components responsible for this separation are four dipole magnets, each bending the ion beam by 30° . As isotopes pass through these magnetic fields, their trajectories are altered according to their mass-to-charge ratio and velocity. Given that the velocities of the produced fragments are relatively similar, their paths are mainly governed by their magnetic rigidity, $B\rho$, where B represents the magnetic field strength and ρ the bending radius. By adjusting the magnetic field B , the system can be tuned to selectively transmit only those isotopes with the desired mass-to-charge ratio, ensuring they follow the correct deflection path through the dipoles.

As a next step in the separation process, the fragments pass through energy-degrading materials, where they lose energy in proportion to the square of their nuclear charge. This energy loss, when combined with the magnetic selection, forms the basis of the FRS's standard separation scheme, known as the $B\rho-\Delta E-B\rho$ method. The standard operation mode of the FRS is an achromatic-mode, which means that despite the momentum spread the fragments are matched at the final focal plane of the separator. This is achieved by the use of a wedge shape degrader with an adjustable angle at F2. Additionally, quadrupole magnets arranged in doublet or triplet configurations at the entrance and exit of each dipole serve to focus the ion beam and maintain optimal transmission conditions. The sextupole magnets correct optical aberrations and improve the resolution.

Identification:

Accurate identification of the produced isotopes is essential for experimental analysis. To unambiguously determine an isotope, both its mass m and atomic number Z must be

measured. This process relies on the basic equation for magnetic rigidity, $B\rho$.

$$B\rho = \frac{p}{q} = \frac{m}{q} c \beta \gamma \quad \text{with} \quad \beta = \frac{v}{c}, \quad \gamma = \frac{1}{\sqrt{1 - \beta^2}} \quad (3.1)$$

For fully ionized isotopes, the charge q is equal to the atomic number Z . The constant c represents the speed of light. By determining the isotope's velocity v through time-of-flight measurements, identifying its charge, and measuring the magnetic rigidity $B\rho$, the mass of the isotope can be calculated.

Time-of-Flight: The velocity of the ions can be determined using time-of-flight (ToF) measurements. For this purpose, scintillator detectors are placed at the focal planes of the separator. The most commonly used measurement is taken between focal planes F2 and the final focal plane, as this segment offers the longest flight path with a lower count rate, improving measurement accuracy.

Magnetic Rigidity: Using a centered primary beam with known $B\rho_0$ value, the magnetic rigidity can be calibrated. The rigidity $B\rho$ of an unknown isotope beam can then be determined by observing the adjustments $\Delta B\rho$ required to center it:

$$B\rho = B\rho_0 + \Delta B\rho \quad (3.2)$$

The deviation of $B\rho$ translates into deviations of the horizontal positions at F2 and F4. Using the dispersion D_{F2-F4} and magnification M_{F2-F4} factors of FRS from the focal planes F2 to F4, Equation 3.2 can be rewritten as:

$$B\rho = B\rho_0 \left(\frac{1 - (x_{F4} - M_{F2-F4}) x_{F2}}{D_{F2-F4}} \right) \quad (3.3)$$

A detailed explanation can be found in [50]. Using the Equation 3.1 in combination with Equation 3.3 enables the determination of the mass-to-charge ratio AoQ by measuring horizontal positions in the focal planes F2 and F4 and the velocity (or more precisely the time-of-flight).

If the beam is not centered, both its position and the system's dispersion must be taken into account for accurate calibration. The trajectory of the beam is tracked using Time-Projection-Chambers (TPC) at the focal planes.

The Atomic Number: The atomic number Z of the ions transmitted through the FRS is determined by measuring their energy loss in Multiple Sampling Ionization Chambers

(MUSIC). These detectors are filled with gas and record the energy deposited by the ions, which is directly related to their nuclear charge. The energy loss of a charged particle passing through matter is described by the Bethe-Bloch formula:

$$-\frac{dE}{dx} = K \cdot Q^2 \cdot \frac{Z}{A} \cdot \frac{1}{\beta^2} \left[\ln \left(\frac{2m_e c^2 \beta^2 \gamma^2}{I} \right) - \beta^2 \right] \quad (3.4)$$

where Q is the charge state of the ion, $\beta = v/c$ is its velocity in units of the speed of light, γ is the Lorentz factor, Z and A refer to the atomic and mass numbers of the absorber material, I is its mean excitation potential, and K is a constant. At the relativistic energies used in the FRS, ions are typically fully stripped ($Q = Z$), and their velocity β is measured independently via Time-of-Flight (ToF). Hence, the energy loss scales approximately with Z^2/β^2 , allowing the nuclear charge to be extracted from the MUSIC signal according to:

$$Z \propto \sqrt{\left(\frac{dE}{dx} \right) \cdot \beta^2} \quad (3.5)$$

3.5 FAIR's Super FRS and FAIR Phase 0

The Facility for Antiproton and Ion Research (FAIR) is currently under construction as an expansion of the existing GSI. Information on the design of the accelerator and the status of the construction can be found on the FAIR websites and recent status reports [51]. FAIR is designed to operate on a significantly larger scale while following a similar conceptual framework as GSI. It includes a large ring accelerator (SIS100, with a circumference of 1100 meters), several experimental and storage rings, and a next-generation fragment separator known as the Super-FRS [40]. The Super-FRS builds upon the design of the original FRS.

Figure 3.5 shows the planned layout of the Super-FRS. Its most commonly used separation mode, $B\rho$ - ΔE - $B\rho$, follows the same principle as in the original FRS: the beam is separated first by its magnetic rigidity ($B\rho$), then by energy loss (ΔE) through degraders—allowing selection based on atomic number Z —and again by magnetic rigidity.

The Super-FRS is designed to handle significantly higher primary and, consequently, secondary beam intensities than the FRS, which is crucial for improving statistics in the study of rare isotopes, reducing experimental run times, and enabling access to more exotic

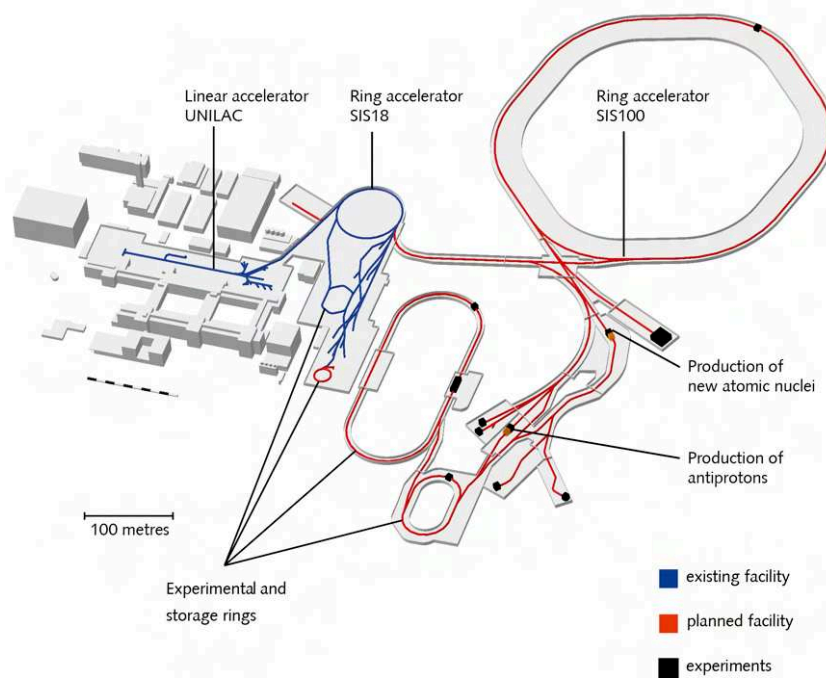


Figure 3.4: Schematic illustration of the existing and planned facilities of FAIR [52].

regions of the nuclear chart. To ensure high-quality separation under these conditions, multiple separation stages are required. This is achieved through a combination of pre-separator and main-separator sections within the Super-FRS. The pre-separator serves to filter out the most abundant, unwanted reaction products and reduce the radiation load on the downstream detectors and magnets. By narrowing down the fragment distribution early in the beamline, it enhances the selectivity and transmission efficiency of the main separator, making it possible to isolate rare isotopes with high precision.

The increase in beam intensity directly impacts the acceptance requirements of the separator. In particular, the higher intensities—especially from fission fragments—necessitate a broader acceptance range. Figure 3.1 presents a comparison of the key parameters between the FRS and the Super-FRS.

The most critical task of fragment separators is to produce and successfully separate rare isotopes. The most exotic rare isotopes have low production cross sections to begin with. In order to expand the boundaries of known isotopes and study properties in exotic areas

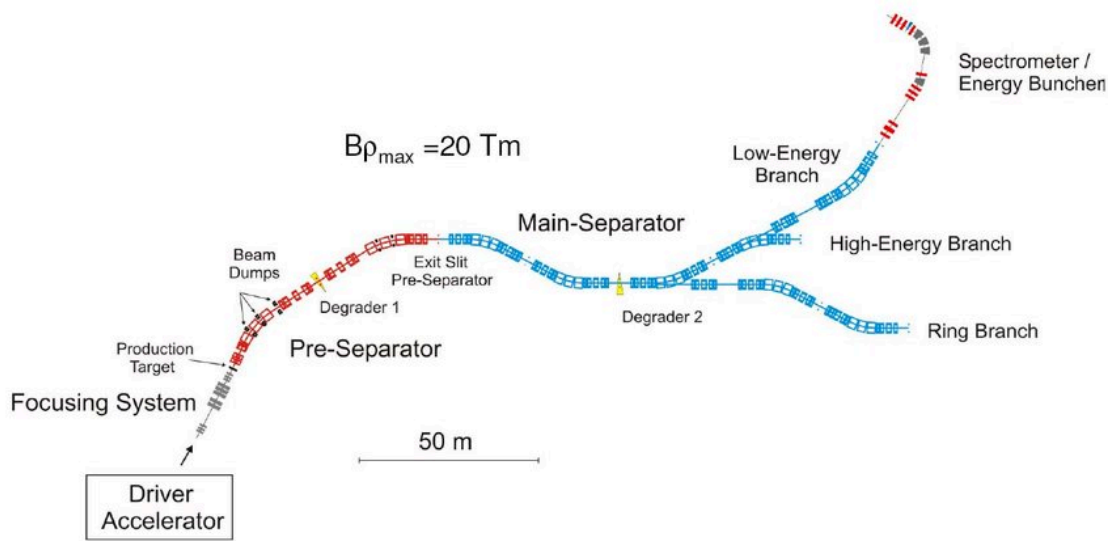


Figure 3.5: Layout of the Super-FRS [53]. The pre- and main separators as well as the three branches are indicated.

of the nuclear chart higher production and transmission yields are of essence for improved statistical results and reduced beam time for experiments.

High-energy beams are typically fully ionized, which, when combined with the multi-stage separation design of the Super-FRS, results in high transmission efficiencies for projectile fragmentation products. Additionally, the large acceptances planned for the Super-FRS will significantly enhance the transmission of uranium fission products. For these products, the expected gain in transmission relative to the FRS is more than an order of magnitude.

Facility	Momentum Acceptance $\Delta p/p$	Angular Acceptance $\phi_x / [\text{mrad}]$	Angular Acceptance $\phi_y / [\text{mrad}]$	Momentum Resolution
FRS	± 1	± 7.5	± 7.5	1500 $\epsilon = 20\pi \text{ mm mrad}$
Super-FRS	$\pm 2.5 \%$	± 40	± 20	1500 $\epsilon = 40\pi \text{ mm mrad}$

Table 3.1: Comparison of FRS and Super-FRS parameters [54].

As shown in Figure 3.6, the transmission gain factors range from approximately 1.5 for heavy nuclei to as much as 16 for lighter nuclei.

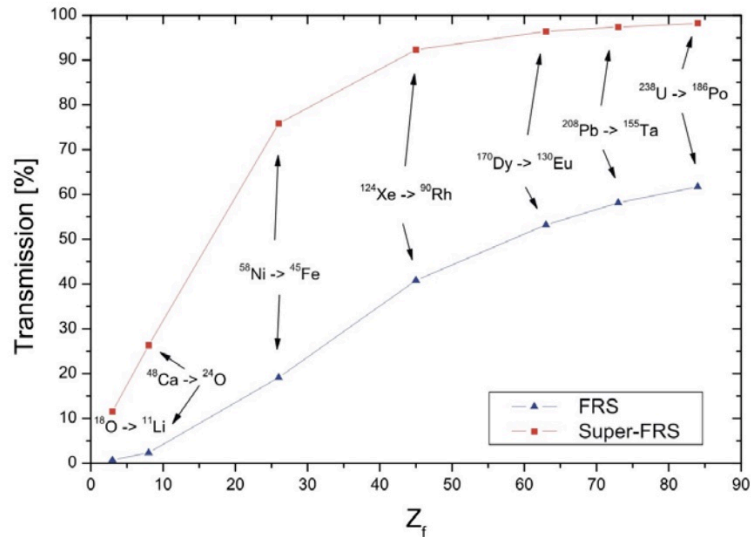


Figure 3.6: Comparison of projectile fragmentation product transmissions: FRS at F4 vs. Super-FRS at MF4 (an end focal plane of the Super-FRS) [54].

In parallel with the construction of FAIR and Super-FRS, several essential upgrades were carried out at the existing GSI facility to meet the future operational requirements of FAIR and to implement necessary modernizations. These upgrades necessitated a temporary suspension of operations at GSI. FAIR Phase-0 represents the initial stage of FAIR's commissioning. It provides a limited research program for the GSI/FAIR scientific community and serves as a platform to commission FAIR detectors as well as upgraded or newly integrated accelerators, such as SIS18 and CRYRING.

4 The Experiment Search For New Isotopes

In the following chapters, the data analysis of the FAIR phase 0 experiment S468 [55], which took place in April 2020 at the fragment separator FRS of the GSI will be described. This chapter will outline the scope and setup of the experiment. The GSI Helmholtz Center for heavy Ion Research will be introduced briefly. The in-flight separation method leading to the particle identification at the FRS will be explained.

4.1 Scope of the Experiment S468

The neutron-rich region of heavy nuclei at the $N = 126$ line is of key interest, particularly for nuclear structure and nuclear astrophysics studies. The S468 experiment was designed to produce isotopes in this partly unexplored region and simultaneously measure key properties for the modeling of the r-process nucleosynthesis: the identification, masses and half-lives. In addition the experiment aims the measurement of cross sections of fragmentation reactions. The production of these isotopes is possible in the fragment separator FRS of GSI applying the in-flight separation technique on projectile fragments of an intense ^{208}Pb beam. In order to achieve particle identification followed by cross section, momentum distribution, as well as mass, half-life, and decay spectroscopy measurements, FRS was operated in combination with new equipment build for FAIR.

A first attempt of identification of new isotopes is described as part of the dissertation of Jan-Paul Hucka [56]. In this work the data analysis for the identification is repeated, in order to ensure that all calibrations, corrections and possible contamination have been removed consistently before claiming the first observations of heretofore unknown nuclides. The data analysis on masses are described in the dissertation of Daler Amanbayev [57]. Based on the particle identification of Jan-Paul Hucka, first attempts to extract beta-decay half-lives are described in the dissertation of Minna Luoma [58]. Data analysis of the S482 experiment that followed the the S468 experiment and used a similar setup was conducted

by Christine Hornung [59]. This experiment focused on developing and applying a novel mean-range bunching technique to study neutron-deficient lanthanide isotopes.

4.2 Experimental Setup

Neutron-rich isotopes close to the $N = 126$ shell closure were produced, separated and identified at the projectile Fragment Separator (FRS, [19]) of GSI. In order to maximize the collection efficiency of the FRS, the SIS-18 synchrotron provided a fully ionized ^{208}Pb primary beam of 1.05 GeV/nucleon, at high intensities of up to 1.5×10^9 ions/spill and spill lengths of 1 – 10 seconds at a repetition rate of 3 – 12 seconds. The fragmentation products produced at the 4 g/cm^2 thick beryllium target at the entrance of the FRS, were separated in-flight throughout the FRS, which was tuned in an ion-optical achromatic mode.

Data was collected throughout four main magnetic rigidity settings that centered the beam on the fully ionized nuclides of ^{205}Au , ^{193}W , ^{193}Ta and ^{190}Lu . While the discovery of the new isotopes was expected for the most exotic ^{190}Lu setting, the other settings were important to connect this setting to well known regions and verify the identification. They were also intended for the measurement of β -decay lifetimes, and nuclear masses around the r-process path. Besides the main settings, several primary beam settings were used for calibration purposes. The magnetic rigidity settings, the spill structure and the duration of the measurement of each setting are summarized in the Table 4.1:

Setting	$B\rho$ in Tm Ta – F2	$B\rho$ In Tm F2–F4	Spill length in s	Pause length in s	Duration
^{205}Au	12.538	10.7348	1	2	6h 2min
^{193}W	12.6853	11.0201	3	2	13h 9min
^{193}Ta	12.904	11.2702	1	2	2h 28min
^{190}Lu	13.117	11.529	0.7s	2.5s	42h 33min

Table 4.1: Main settings of the S468 experiment. The given durations do not include the tuning of FRS.

The FRS and its detector systems used in this experiment are depicted schematically in figure 4.1. A 223 mg/cm^2 thick niobium backing of the target ensured that the heavy fragment products were almost all completely ionized, which aided identification. On the trajectory from the target to the final focal plane, F4, the reaction products were

spatially separated according to the $B\rho$ - ΔE - $B\rho$ method: Exiting the first two magnetic dipole sections, the reaction products are horizontally separated according to their mass-to-charge ratios, when they arrive at the second focal plane, F2, where a degrader system, consisting of a disc and a wedge, is installed. The different, position and charge dependent energy losses of the fragments in the degrader allow a second stage of separation in the third and fourth magnetic dipole sections. Hence, the focus of each isotope is spatially separated at F4.

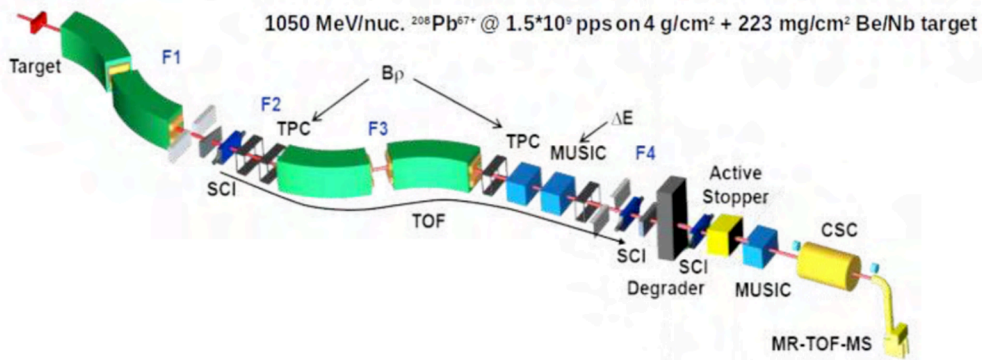


Figure 4.1: The experimental setup of the FRS from the target to the final focal plane during the S468 experiment. The main detectors consisting of the plastic scintillators (SCI) for time-of-flight measurements, time projection chambers (TPC) used for position measurement and $B\rho$ determination and MUSIC detectors for charge measurements are shown. At the final focal plane the active stopper for beta-decay measurements and the FRS Ion Catcher with its cryogenic stopping cell (CSC) and mass spectrometer (MR-TOF) are visualized.

The identification of particles was achieved by the event-by-event measurement of their charge, Z , and mass number, A . For charge measurements, Multiple Sample Ionization Chambers (MUSIC, [60]) filled with P10 gas were used in the energy loss mode. In the MUSIC detectors the energy loss was recorded by eight consecutive anodes and the geometric mean of all eight measurements was used to improve the resolution. Velocity calibration, horizontal position corrections at the edges, and stability corrections were applied to the raw signals. The region of interest for this experiment was on the heavy part of the nuclear chart. In this region charge states have to be taken into account and handled carefully in order to obtain clear spectra. The mass number, A , was derived from magnetic rigidity analysis and time-of-flight measurements that led to the mass-over-charge ratio,

AoQ. Knowledge of the trajectory is required for magnetic rigidity analysis. Time Projection Chambers (TPC, [61]) were used for position measurements. The TPCs measure the drift time of electrons produced by charged particles ionizing the atoms of the P10 gas, while passing through the detector. The TPCs have four anodes on the bottom-side along the beam line and two independent delay lines on the front and back sides. With respect to the beam line, a vertical drift of the electrons is achieved by a uniform electric field inside the detector volume. From the measurement of the drift time of the electrons, the vertical position of the charged particle is calculated. The time difference between the arrival of the signal on the left and right side of the delay line is measured to determine the horizontal position. The TPCs can measure the vertical position four times and the horizontal position two times. Since the total delay line is fixed, the vertical and horizontal positions are correlated as shown in 4.1:

$$t_{CS} = t_l + t_r - 2t_d \quad (4.1)$$

where t_l and t_r are the times from the left and right of the delay line, t_d is the drift time and t_{CS} is called the control sum. Putting restrictions on the control sum is used to reduce the noise. Two TPCs were placed in both F2 and F4, which allowed a particle tracking with positions and angles in both the horizontal and vertical planes. The time-of-flight from F2 to F4 was measured using plastic scintillators installed in both focal planes. Path-length corrections were applied to the resulting mass-to-charge ratios. Position-dependent corrections of AoQ were implemented in F2 and F4 to mitigate the effect of burned spots on both the F2 and the F4 scintillators. Adjusting the thickness of the degrader in F4, the isotopes were implanted either in the FRS Ion Catcher [62] for mass measurement or in the active stopper [63], a detector system consisting of two layers of double-sided silicon strip detectors capable of measuring implantation and subsequent β decays surrounded by eight LaBr3 detectors for γ -spectroscopy.

5 Data Analysis

Throughout the experiment data were collected under four distinct FRS settings, each optimized to maximize the intensity of one of the following isotopes: ^{205}Au , ^{193}W , ^{193}Ta , and ^{190}Lu . New isotopes were expected in the most exotic setting ^{190}Lu .

Setting	Start (Date)	Start (Time)	End (Date)	End (Time)	Duration
^{205}Au	11.04.2020	14:25	11.04.2020	20:27	6h 2min
^{193}W	12.04.2020	21:12	13.04.2020	10:21	13h 9min
^{193}Ta	16.04.2020	19:37	16.04.2020	22:05	2h 28min
^{190}Lu	17.04.2020	20:15	19.04.2020	14:48	42h 33min

Table 5.1: Measurement periods for different FRS settings.

Several calibration and correction steps were performed consistently in all settings to achieve unambiguous isotope identification and reduce background noise. In this chapter the identification of the atomic number Z and the mass number A —deduced from the mass-to-charge ratio A/Q —will be explained in detail. All the analysis steps carried out—calibrations, corrections and the charge state selection—will be described.

5.1 Identification of the Charge Z

MUSIC detectors were used to measure the charge or charge states of the isotopes. MUSIC detectors are well suited for precise nuclear charge (Z) measurements because they determine the ion's energy loss (dE/dx) in gas, which scales approximately with Z^2 according to the Bethe-Bloch formula, as described in Equations 3.4 and 3.5. Unlike for instance scintillators, which exhibit strong non-linearities and velocity-dependent quenching effects in their light output, MUSIC detectors provide a linear and stable response across a wide range of velocities. Their multiple sampling structure further

improves resolution by averaging out fluctuations, making them ideal for distinguishing neighboring high- Z nuclei in relativistic heavy-ion experiments. The ionization chambers were operated in energy loss mode, which meant that they recorded energy loss caused by the charged particle flying through the gas filled chamber. As charged particles pass through the MUSIC detector, they ionize the gas atoms along their path, producing electron-ion pairs. The total number of electrons collected at the anodes is proportional to the energy lost by the particle via ionization. According to the Bethe-Bloch formula (Eq. 3.4 and Eq. 3.5), this energy loss is proportional to the square of the charge of the particle and inversely proportional to its squared velocity. In order to extract the atomic number Z from the raw MUSIC signal and improve the resolution, several calibrations, corrections, and charge state selection have to be applied. In the following paragraphs, these analysis steps will be described and discussed.

Velocity Calibration: The energy loss of charge particles inside the MUSIC depends not only on the charge but also on the velocity of the isotope passing through. In order to extract the information on the charge, the velocity dependence of the detector response was taken into account. Calibration runs with the primary beam at five different energies that were performed at the beginning of the experiment were analysed—summarized in Table 5.2. A second-degree polynomial calibration curve was fitted to the detector signals for each velocity measurement. The same calibration parameters were used for all FRS settings to calculate the charges. The second-degree polynomials and the resulting calibration parameters are displayed in Figure 5.1 and Table 5.3.

Primary Beam Energy in MeV/nucl.	$B\rho$ in Tm	β in c	ΔE MUSIC41 in arb. units	ΔE MUSIC42 arb. units
600	9.731	0.777	3343	3247
670	10.507	0.800	3190	3088
750	11.354	0.822	3060	2955
925	13.135	0.858	2870	2759
1050	14.369	0.877	2772	2656

Table 5.2: MUSIC41 and MUSIC42 raw signals for different primary beam energies.



Figure 5.1: Velocity Calibration of MUSIC41 in orange and MUSIC42 in blue. The pulse height of the MUSIC detectors were measured at five different velocities of the primary beam. The results of this measurement are shown in the Tabela 5.2. Second order polynomials were fitted to determine the calibration factors (Table 5.3).

Detector	a	b	c
MUSIC41	11476	24862	15636
MUSIC42	11392	24535	15528

Table 5.3: Velocity calibration parameters for the MUSIC detectors determined by fitting second degree polynomials $-ax^2+bx+c$ to the pulse heights of measurements of the detectors at five primary beam velocities (Figure 5.1).

Position Correction: The position dependence of the MUSIC detectors was then studied and corrected. The position dependence was visualized using the horizontal distribution of fission fragments that were present during each setting and covering the entire horizontal plane of the MUSIC detectors (Figure 5.2). A fission product produced during the ^{193}Ta setting with high rates was selected. The position correlation visible at the edges of the MUSIC detectors can be explained by higher electron recombination probabilities at the edges compared to the midsection, due to slight electric field inhomogeneities or gas impurities. The ratio of number of electrons collected to number of electron-ion pairs produced is lower at the edges. The horizontal position in the MUSICS was divided into three sections: the edges where a position correlation was observed and the middle section,

with no position dependency of the signal. Three functions with smooth transitions at the borders were fitted to these three ranges (third- and second-degree polynomials at the edges and a constant at the mid-section). The resulting fit is shown in red in Figure 5.2. The MUSIC signals on the edges were corrected with a position-dependent factor and leveled with the position-independent midsection. The same correction parameters were used consistently for each FRS setting. Using position and angle measurements of both TPCs, and the MUSIC distances the position of the particles at the detectors were determined. Since the correction are applied using factors, the exact knowledge of the MUSIC distances was not relevant for the correction.

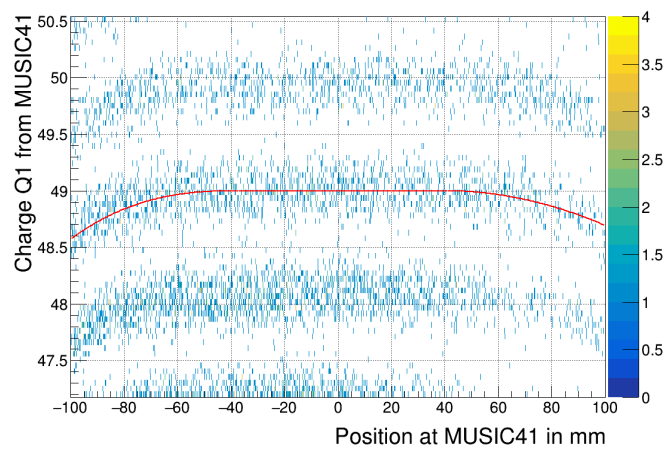


Figure 5.2: The red curve was fitted on the MUSIC41 signal of a fission fragment from the ^{193}Ta setting. The signal was corrected on the edges by a position dependent factor to level the sides with the constant mid-section.

Stability Correction: In addition to velocity and position correlations, a time dependence was introduced to the raw MUSIC signals due to variations in environmental temperature and pressure throughout the longer measurements (2.5 h-42.5 h). The duration of the different settings is summarized in Table 5.1. The longest measurement run corresponded to the most exotic setting, optimized for ^{190}Lu , which exhibited the lowest rates. This setting was expected to yield new isotopes, necessitating an extended measurement duration. Fluctuations in temperature, T , and pressure, P , affect the signal because according to the Bethe formula, the energy loss is also proportional to the gas density. Assuming

ideal gas behavior for the P10 gas in the MUSIC detector, the density is proportional to $\frac{P}{T}$. Figure 5.3 shows the resulting variations in pulse height during day and night affect MUSIC signals during ^{190}Lu . The wave-shaped form of the signals worsen the resolution and complicate the separability of the charges. A time-dependent offset was added to the MUSIC signal every 1000 s to counteract the instability.

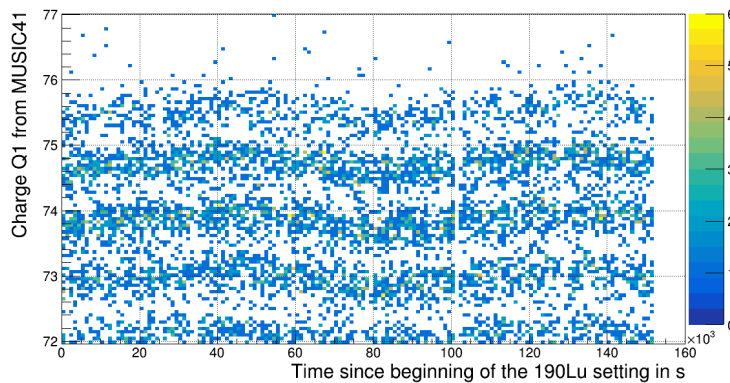


Figure 5.3: MUSIC41 signal during ^{190}Lu setting before the stability correction (beginning of setting at 14:48 in the afternoon). The waves shaped by slight rises and falls of the signal show the day- and night-time effects. The signal was corrected with time dependent offsets every 1000 s.

The stability and position corrections applied to the MUSICs improved the separation of the different charges. The position correction had a significant effect on the charges that arrived at the edges of the MUSICs, where most of the "new isotopes" are expected (green curve in Figure 5.4). The stability correction led to an improved separation of all charges (blue curve in Figure 5.4).

Charge State Selection: In order to achieve unambiguous particle identification, it is important to separate and clean the charge states of isotopes that are created when the fragments fly through matter. A fully ionized primary beam is supplied to the FRS by the SIS18. Most of the charge states of the fragments produced in the target are suppressed by the stripper directly at the exit of the target. Yet a fraction of (mostly) hydrogen-like charge states remain. When the fragments fly through the FRS they pass through matter. The most dominant matter present inside the FRS is the 2000 mg/cm^2 aluminum degrader.

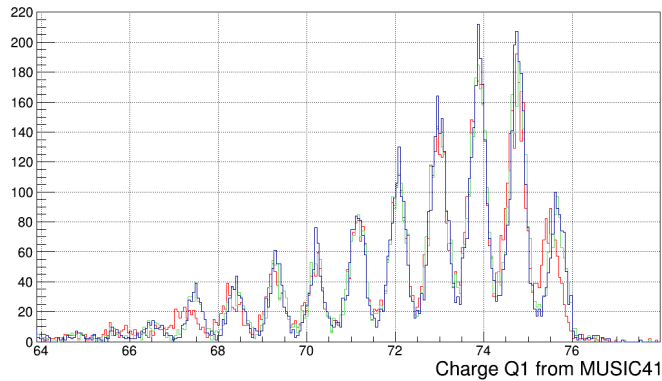


Figure 5.4: The charge distribution measured by MUSIC41 during the ^{190}Lu setting. The charge after velocity calibration of the MUSIC signal is shown in red. A step by step improvement of the separation of the peaks is observed after adding the position correction (green curve) and then the stability correction (blue curve).

Charge state estimations for Au isotopes at 800 MeV/nucl. inside the stripper and degrader are listed in Table 5.4

Material	Thickness in mg/cm^2	Fully ionized	H-like	He-like
Nb	225	92.3 %	7.5 %	0.2 %
Al	2000	82.7 %	16.5 %	0.8 %

Table 5.4: GLOBAL charge state estimations [64] for 800 MeV/nucl. Au isotopes inside the stripper (Nb) and the degrader (Al).

According to the probabilities shown in Table 5.4 there is a 7.5 % probability for the Au isotopes exiting the stripper H-like. At the degrader, 83 % of these H-like Au isotopes will lose the electron and continue their path fully ionized until they reach the final focal plane. Multiplying the two probabilities results in 6 % of the original Au isotopes. These will be referred to as [1,0] charge states, because they fly through the first half of the FRS H-like and continue fully ionized through the second half. On the other hand, the isotopes have a 92 % chance of flying through the first half of the FRS fully ionized, but 17 % of these isotopes will pick-up an electron in the degrader. These cases are referred to as [0,1] states and consist of 15 %. The [1,0] and [0,1] charge states are the most commonly observed charge states for heavy ions in the FRS. The probability of creating

charge states inside the FRS material drops with for lower atomic numbers. In the S468 experiment the Au isotopes measured during the Au and W settings were the isotopes with the highest atomic numbers included in the data analysis. For all other isotopes analyzed in this thesis lower probabilities are expected. The gates and selection applied to the data will be explained in the following.

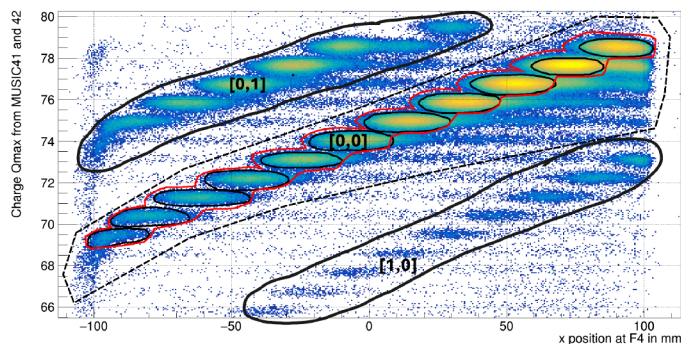


Figure 5.5: Charge state selection in the ^{193}W setting: The charge states of the fragments are spatially separated at F4. The different cuts that were used to select the [0,0] states are shown. The [0,1] and [1,0] states are visible, respectively on the upper and lower sides. For charge state investigation purposes and to avoid cutting into the [0,0] states, three kinds of cuts with different levels of stringency were applied: a broad cut shown in black dashed lines, a tighter cut around the [0,0] states shown in red, and one by one selections of each atomic numbers [0,0] state, encircled in black. The effect of the application of the cuts will be discussed in the following paragraphs.

The energy loss inside the degrader depends on the charge, which means that the energy loss of each charge state inside the degrader is different. For the [1,0] and [0,1] states this translates into a horizontal separation from the [0,0] states in opposite directions at the final focal plane. This effect can be observed in Figure 5.5 showing the F4 position vs the charge measured in MUSIC41. The [0,1] states follow the same trajectory as the [0,0] states in the first half of the FRS. After picking up an electron in the degrader their charge changes which sets them on a different trajectory in the second half. This is observed when horizontal positions at F4 are plotted against the charges measured by MUSIC detectors, while the [0,0] states are aligned on a diagonal in the middle the [0,1] states positions were shifted to the left. The [1,0] states on the other hand arrive at F4 shifted to the right of the [0,0] states. Selection cuts were applied to the area containing the [0,0] states for

further analysis. The three different cuts applied to study and clean contamination in this area without reducing the statistics of [0,0] states are drawn in Figure 5.5. The first broad cut surrounds the area between the [0,1] and [1,0] states. While the dominant charge states—namely the [1,0] and [0,1] states—are suppressed with this selection contamination remain especially for in the higher charge regions. One example are the [1,1] states. With this selection they remain inseparable from the [0,0] state of the higher atomic number. There are visible contamination within the broad selection, particularly for higher charges. These can for instance be attributed to secondary reactions in the degrader, such as neutron evaporation as was suggested in [65]. Applying tighter selection at the risk of losing statistics most of these contamination can be eliminated.

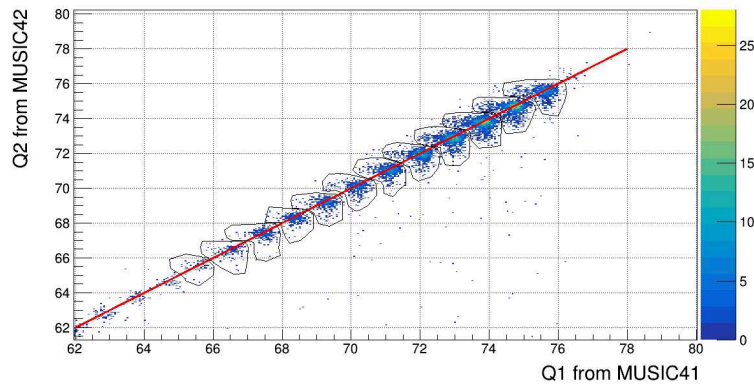


Figure 5.6: Boomerang selection and ID line correction in the MUSICs for the ^{190}Lu setting: For each charge a boomerang selection was made to include electron pick-up/ loss in either MUSIC and Z was defined as the maximum value between Q1 and Q2. The cuts are visualized in black. Q2 was aligned with Q1. The ID line ($Q1=Q2$) is depicted in red.

To identify and correct some of the [1,1] states, two MUSIC detectors were used back to back with a stripper between. Most of the [1,1] states incorrectly identified in the first MUSIC would lose their electron in the stripper. A correct identification in the second MUSIC would follow. Some correct identifications of the first MUSIC would be falsified in the second MUSIC as some of them would pick up an electron in the stripper. The cases of electron pick-up or loss are visualized, when the charge measured in the first MUSIC, Q1, is plotted against the second, Q2 (Figure 5.6). In this plot, boomerang-like shapes are visible for each charge. After aligning the charge measurement from the second MUSIC with the first, by fitting a linear line through the mid-sections of the boomerang shapes,

representing the $Q1 = Q2$ cases, and correcting $Q2$ accordingly, a boomerang shape was selected for each charge and Z was defined as the maximum value between $Q1$ and $Q2$. The charges were then selected by applying one of the tight $[0,0]$ charge state selections shown in Figure 5.5. For the ^{193}W setting the one by one selection for each charge was used. Additionally the "boomerang-selections", like the ones shown in Figure 5.6 were used to group and identify the charge.

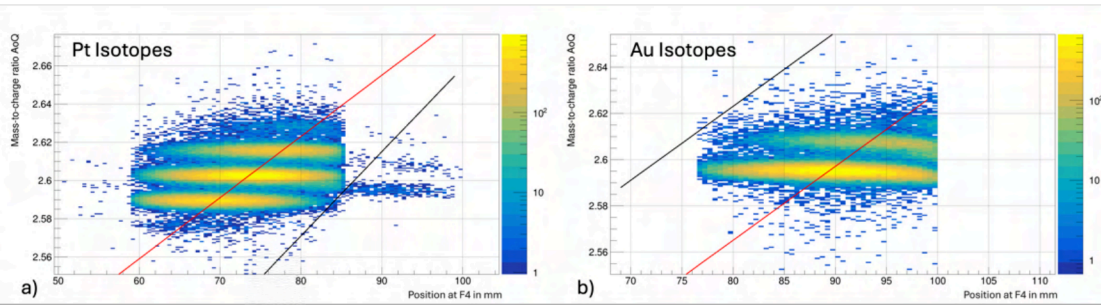


Figure 5.7: AoQ vs. F4 horizontal position of Pt isotopes in a) and Au isotopes in b) measured during the ^{193}W setting. LISE++ was used to determine the right and left-side edges of the position distributions for each isotope of every atomic number. The black line in a) corresponds to the linear fit applied to the simulated right-side edges of the Pt isotopes ($Z = 78$, the red line in a) shows the left-side distribution of Au isotopes $Z = 79$. The black line in b) is the same as the red line in a). The red line in b) shows the left-side edges of Hg isotopes $Z = 80$.

Further contamination is visible in the mass-to-charge ratio (AoQ) vs. F4 x-position spectra for each selected charge (Figure 5.7). The identification of AoQ will be described in the following section 5.2. The LISE++ simulation program [66] was used to define the edges of the F4 positions for each isotope of a selected charge. A linear line fitted to the edges of the positions according to LISE++ was used to set a gate and eliminate the majority of these remaining contamination. These contaminants can be explained by $[0,0]$ charge states that pick up an electron before or in the first MUSIC. Their charge measurement in the MUSIC is decremented by one, but their AoQ measurement and x4 position correspond to the correct measurements of the $[0,0]$ states. They are identifiable in the AoQ vs. F4 position plots of each charge (as groups with AoQs in between to isotopes and x4 positions shifted), and a majority of this contamination is removed by applying the aforementioned LISE++ simulation gate. The part overlapping in position with the neighboring charge is more complicated to remove. For the ^{190}Lu setting, manual

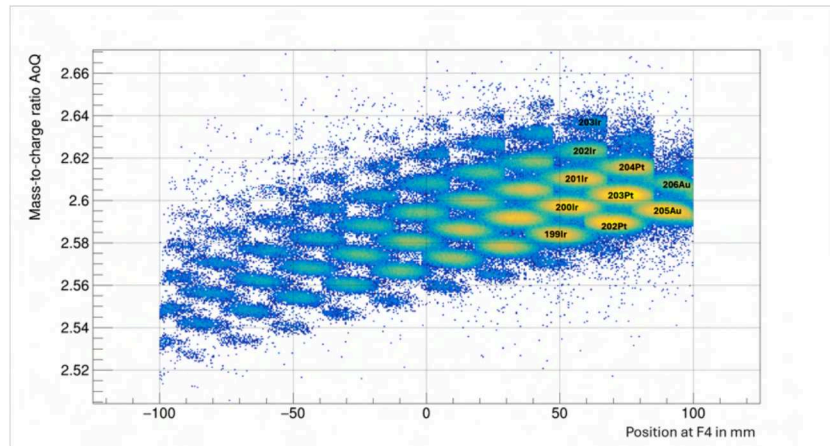


Figure 5.8: AoQ vs. F4 horizontal position of all isotopes and for all charges plotted together. The parts of neighboring charges overlapping position are visible.

cuts were applied to each isotope and ambiguous data were not included to ensure that contaminants were removed from the new isotope statistics without losing too much statistic. For the ^{193}W setting, where the main objective was to anchor the identification for all settings, and where enough statistics were available, a different approach was used. A similar LISE++ simulation was used to determine the edges of the position distributions of the isotope, this time on the left side. A linear line was fitted for each charge. The line was used as a gate to remove all the contaminated parts of the neighboring isotopes $Z - 1$ —including close to half of the statistics for each isotope. The red line in Figure 5.7a) was used to eliminate all the contaminated part from the Pt isotopes, $Z = 78$, (along with half of the statistics). This line corresponds to the left-side edges of the Au isotopes, $Z = 79$, according to LISE++ and is shown again in Figure 5.7b) in black on the left side of the Au isotopes. The red-line in Figure 5.7b) shows the gate used to clean all contaminated parts from Au isotopes using the LISE++ simulation for the left-side edges of neighboring Hg isotopes $Z = 80$.

As is evident from Fig. 5.4 as well as the following particle-ID plots, the centroids of the charges do not align with the expected integer values, and the spacing between adjacent charges deviate from one, as well. This effect is a result of the non-perfectly linear detector response and can be overcome by applying a general recalibration factor. Instead of introducing an ad-hoc recalibration, it is possible to point out that the charge identification of the ions is unambiguous due to the following reasons: (i) As part of the calibration runs, $^{208}\text{Pb}^{82+}$, $^{208}\text{Pb}^{81+}$, and $^{208}\text{Pb}^{80+}$ have been transported through and identified in the

FRS. Charge-79 ions from the ^{205}Au setting connect directly to these Pb charge states. (ii) Experiments with the FRS Ion Catcher unambiguously identified the masses of $^{204,205}\text{Au}$ in the relevant setting [57].

5.2 Identification of the Mass over Charge Ratio AoQ

To calculate the mass-over-charge ratio of the fragments magnetic rigidity calculations, based on the tracking of the fragments with two TPCs at F2 and two at F4 providing position and angle information on both focal planes were used. In addition, the time of flight of transmitted fragments was measured from F2 to F4 with plastic scintillators in both focal planes. Both scintillators at F2 and F4 had burned spots during the measurements. After investigating the burns, as well as the effects of the burns on the mass-over-charge measurement, position-dependent corrections were implemented on the measured mass-over-charge ratio at F2 and at F4. The following procedure was followed, in order to

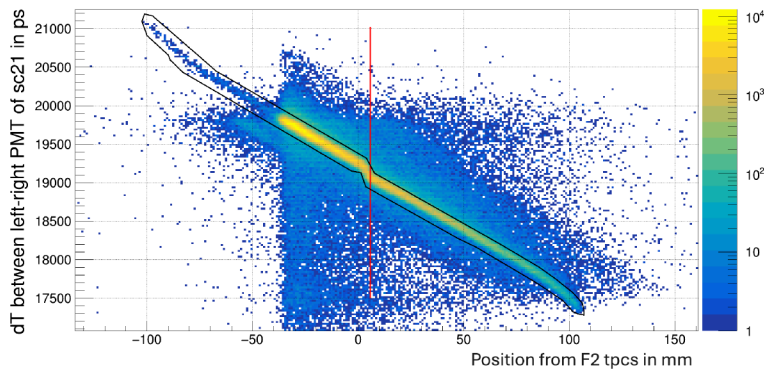


Figure 5.9: The location of the scintillator damage was identified when the position measured by the TPCs was plotted against the time difference recorded between the left and right PMTs of the scintillator. A linear correlation is expected in a homogeneous scintillator that provides a constant signal propagation velocity. The shape of this plot and the location of the burn (red line) were identical in all the settings.

ensure consistency between settings. The ^{193}W setting was used to investigate burns in the scintillators, because in addition to high statistics, the fragments produced during

this setting had the widest horizontal spread in both focal planes, allowing a position-dependent study of burns and their effects. The time difference between the left and right photomultiplier tubes (PMTs) of the scintillators was converted to position and compared with the position predicted by the TPCs in the corresponding focal planes. Based on this comparison, the burned spot of the F2 scintillator was located. Although a linear correlation is expected when the position according to the scintillator is plotted against the position measured by the TPCs, a parallel shift was observed for the F2 scintillator close to the centre (Figure 5.9). This visualization of the burned spot was reproduced for all settings. Linear functions fitted to both sides of the burned spot using the data from the ^{193}W setting were compatible in all settings. The correlation between the positions predicted by the TPC and measured with the burned F2 scintillator had the same shape, including the parallel shift occurring at the same spot. Next, the AoQ distribution of a selected charge was plotted against the position at the scintillator (measured by TPCs). Although on one side of the scintillator the mass-to-charge ratios did not show a correlation with position, a tilt was observed in the burned spot followed by a slight negative linear correlation on the other side (Figure 5.10). The position correlation on the burned side was parallel for all mass-to-charge ratios throughout the different settings and was corrected with a position-dependent factor.

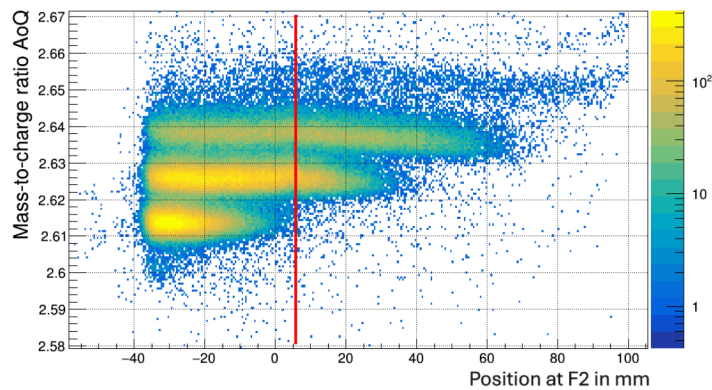


Figure 5.10: The effect of the scintillator burn on the AoQ measurement. The AoQ measurement was corrected with a position-dependent factor, determined by a linear fit applied on the affected side of the scintillator. As the slope on the damaged side was consistent in all settings and parallel for all AoQ ratios, the same factor corrected the AoQ ratios for all settings equally.

The same procedure was applied to investigate scintillator damage in F4. The plot comparing the position measurement of the TPCs and the scintillator in F4 is shown in Figure 5.11. Instead of a parallel shift after a clearly noticeable tilt occurring at the damaged spot of the scintillator as in F2, a smooth but significant change in the slope of the correlation is observed at F4. In other words, the velocity of the signal propagation was not uniform on the two sides of the scintillator.

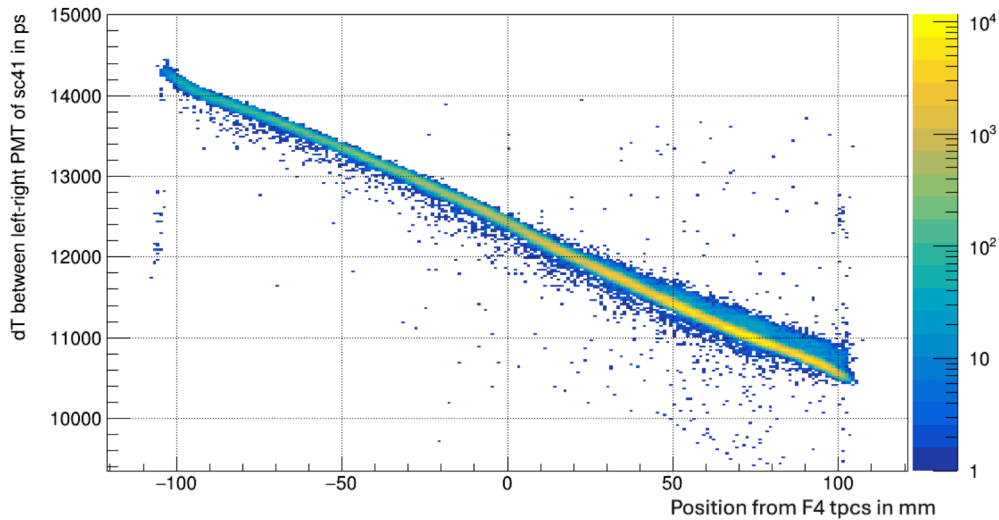


Figure 5.11: The position measured by the TPCs plotted against the time difference recorded between the left and right PMTs of the scintillator at F4. The variation of the slope on each side of the scintillator indicates a non-uniform propagation velocity of the signal inside the scintillator. The shape of this plot was identical in all the settings.

This resulted in a visible discrepancy between the AoQ measurements recorded on each side and explained the observed change in gradient in the identification plots (5.14 of the experiment settings that was complicating the identification. According to LISE++, the F4 position distribution of the mass-to-charge ratios of isotopes that follow the "Z-1, A-3 pattern" and form a line in the identification plot is described by a second degree polynomial (black curve in Figure 5.13). In the data from the experiment this distribution was expressed by different quadratic functions for each side of the scintillator (red and purple curves in Figure 5.13), both significantly deviating from the simulation. Comparing the fit applied to the ^{193}W data with the F4 position distributions of the other settings

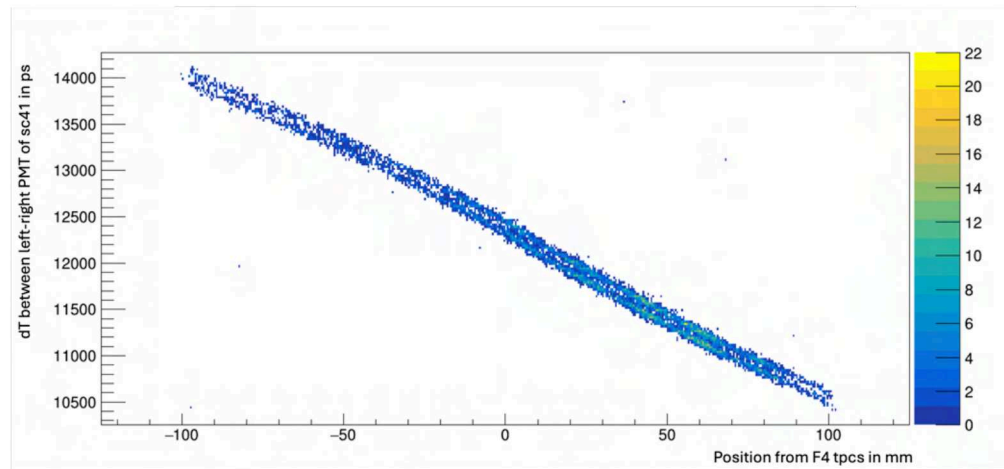


Figure 5.12: The TPC versus scintillator plot recorded during the ^{190}Lu setting. The double structure caused by a jump in the scintillator signal. This deteriorated the AoQ resolution. The correction is discussed in the text.

showed that despite the damaged scintillator, the distribution was parallel for all "Z-1, A-3" lines across all settings. The same position-dependent quadratic corrections were applied to all settings to match the LISE++ simulation. Consequently, the change in slope in the identification plot that challenged the consistent identification across the different settings was corrected.

During the investigation of scintillator damage in F4, a double structure was detected in the TPC versus scintillator plot recorded during the ^{190}Lu setting. A scan of the plot over time showed that the scintillator signal shifted from one event to the next during the measurement. The jump in the scintillator signal, unnoticed during the experiment, shifted the AoQ measurement, which resulted in a deterioration of the resolution in the combined measurement before and after the jump. Applying an alternative way to calculate the time of flight restored the resolution. During the experiment, the time of flight is recorded as the time difference between the left PMTs of the scintillators at F2 and F4 and between the right PMTs. The raw time difference from left-to-left or from right-to-right does not account for the time the signal propagates through the scintillator from the position of the event to the PMT on either side. In the usual approach, the geometric mean of the left-to-left and right-to-right signals is calculated, which removes the position dependence for scintillators of equal dimensions and material. Alternatively, the left-to-left signal can be combined with the position information from the TPCs to calculate the time of flight.

The latter approach was not influenced by the sudden scintillator jump in F4 and was therefore selected as the method to calculate the time of flight for all settings.

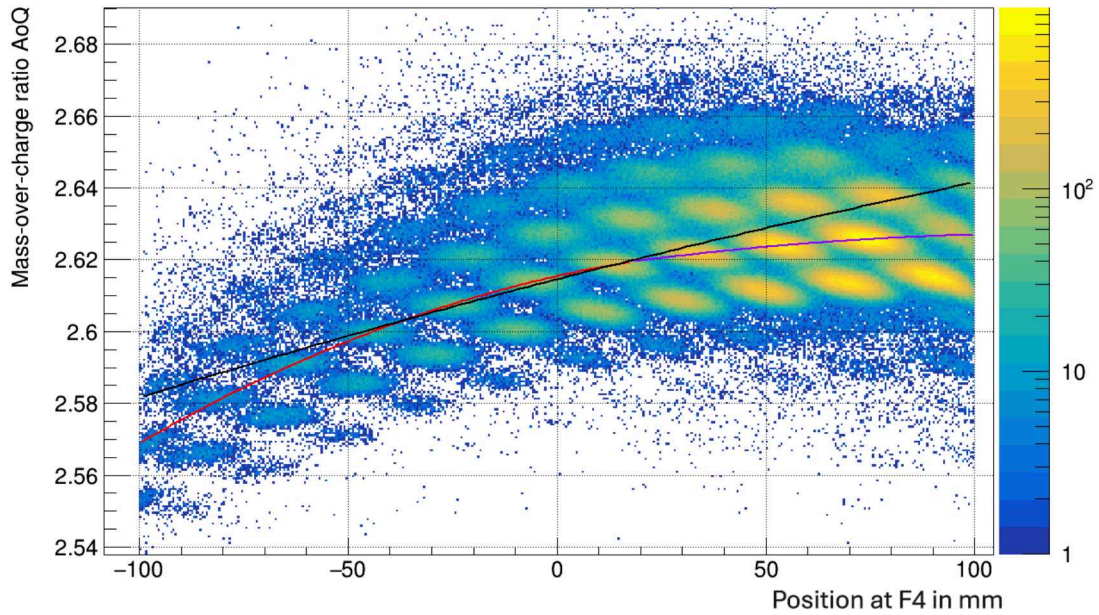


Figure 5.13: The effect of the scintillator burn at F4 on the AoQ measurement. Second order corrections were applied on both sides of the scintillator (red and purple curves) to match the distribution to the LISE++ simulation (black curve). The fit on the position distribution of AoQ was consistent in all settings. The correction parameters were used for all settings.

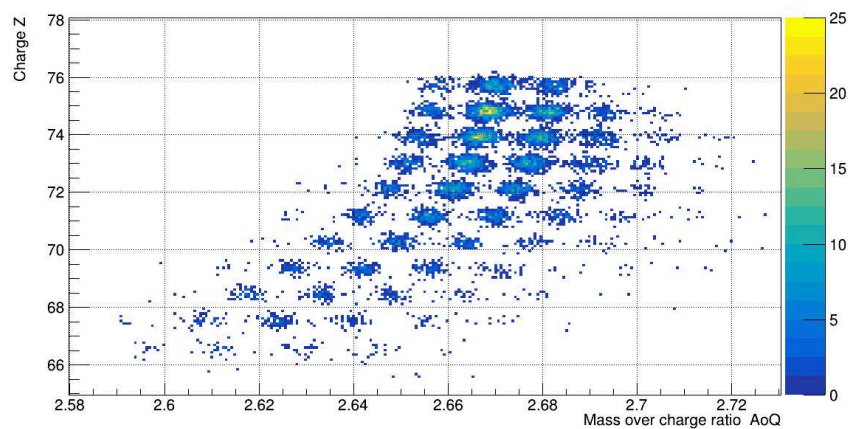


Figure 5.14: The ID plot before the position correction at F4 from the ^{190}Lu setting. A change in the slope is observed. As a consequence, the mass-to-charge ratios for the different isotopes yield inconsistent values

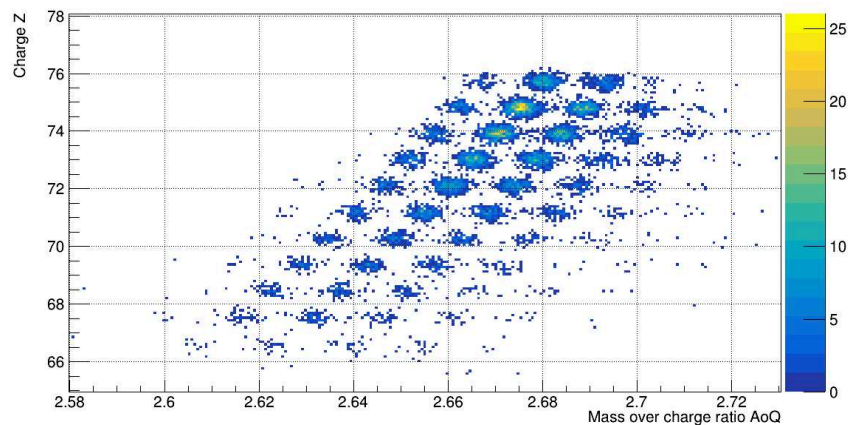


Figure 5.15: Identification plots after the F4 position correction of the mass-over-charge ratios from the ^{190}Lu setting. The discontinuity in the ID plot disappears after the position correction in F4.

5.3 Gates for Background Reduction

In addition to the mentioned correction and calibration steps and charge state selection, gates were applied to the data to suppress the background. Vertical position gates (Y2-gates) in F2, reduced events that could not have been transmitted through the FRS. If such events are detected in F4, they can be attributed to pile-up occurrences. Restrictions on the control sum (described in equation 4.1) were applied to the F2 TPCs to reduce noise likely to occur when the rates are high. In Figure 5.9 the position measured by the F2 TPCs is plotted against the position according to the F2 scintillator. Events outside the black border predominantly represent background noise, as this plot compares the position measurement at the scintillator recorded by two different detectors. The checksum and F2-position gates showed a significant effect for the two settings with higher rates, ^{205}Au and ^{193}W .

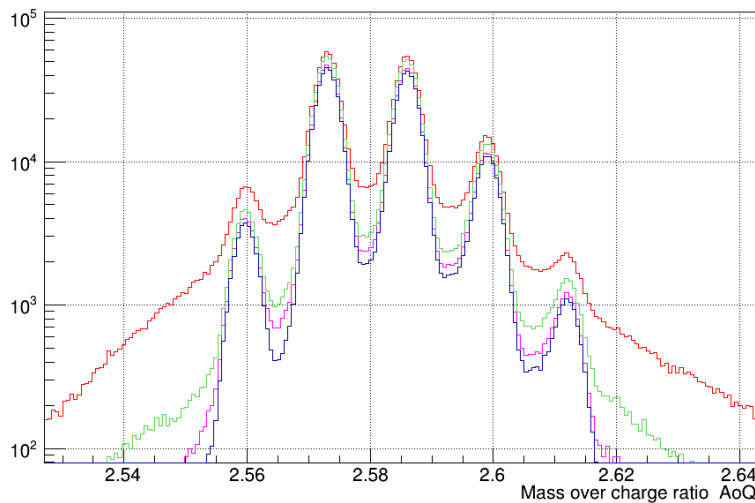


Figure 5.16: AoQ, Pt Isotopes in Au setting. red: no gates, green: Y2 gates, pink: Y2 gates + checksum gates, blue: Y2 gates + checksum gates + f2 position gates

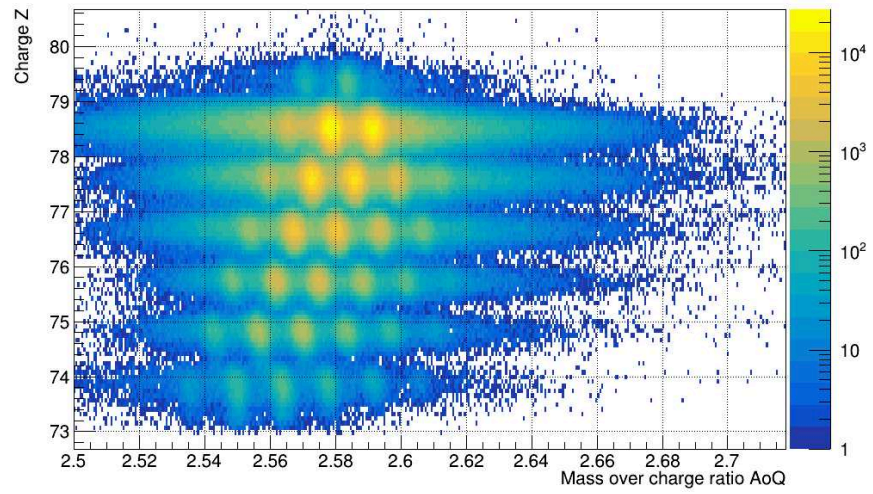


Figure 5.17: ID plot of Au setting before gates.

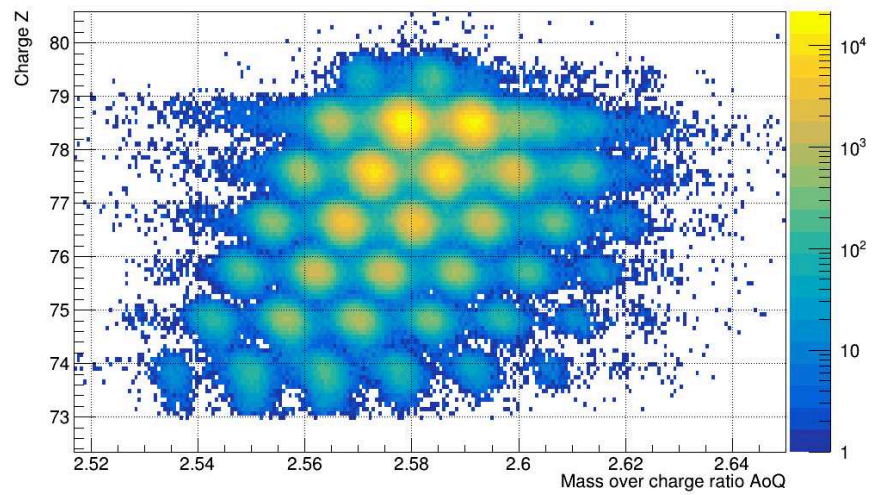


Figure 5.18: ID plot of Au setting before gates.

5.4 Assignment and Counting of the Identified Isotopes

After all calibrations, corrections, charge state selections, and necessary gates were applied to the data, identification plots were processed sufficiently, allowing for the assignment of isotopes.

Two different methods were carried out and compared to complete the identification. In the first method, the known theoretical mass-to-charge ratios of the primary beam in the calibration settings was compared to the measured mass-to-charge ratio after the previously mentioned steps of calibration and correction. A shift was applied to the AoQ measurement in all settings in the form of an offset that fixed the AoQ measurement in the primary beam setting to its theoretical value. The second method compared the settings with LISE++ simulations and looked for isotopes on the $N = 126$ line, such as ^{205}Au in the setting of ^{205}Au or ^{205}Au and ^{204}Pt in the setting of ^{193}W .

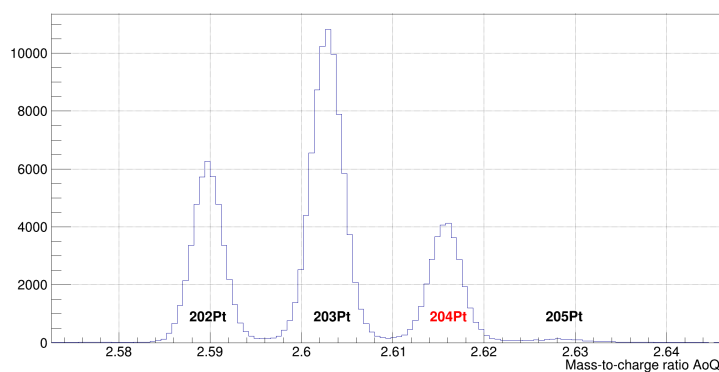


Figure 5.19: The mass-to-charge ratio AoQ of Pt isotopes in the ^{103}W setting. After the $N = 126$ isotope ^{204}Pt , a significant drop is observed. Furthermore this drop can not be explained by a drop in transmission, since according to LISE++, the transmission probability of ^{205}Pt (21.89%) is higher than for ^{204}Pt (14.98%).

The $N = 126$ line is recognizable in the ID plots, because a significant drop of rates is observed after these isotopes, which cannot be explained with a drop in their transmission percentages through the FRS. In the ^{193}W setting, a drop was observed after all $N = 126$ isotopes that were measured (^{203}Ir , ^{204}Pt , and ^{205}Au). However, $N = 126$ was best

recognizable in the Pt isotopes, where an indicative drop in statistics was detected after the ^{204}Pt even though—according to LISE++—its neighboring $N + 1$ isotope ^{205}Pt had a considerably higher transmission probability, with 21.89% for ^{205}Pt compared to 14.98% for ^{204}Pt .

Recognizing one isotope in each setting allows to identify all others from their relative position. To verify and ensure consistency in the identification across settings ^{193}W in the setting ^{193}W fixed to its theoretical value, the resulting change was applied to all settings, including the primary beam setting. For both methods (1. anchoring the primary beam and 2. anchoring ^{193}W in the ^{193}W setting), the identification was compatible for all settings as the theoretical mass-to-charge ratios were for all cases within the region of the peak of the corresponding isotopes. Fixing the identification according to the primary beam, as explained in the first method, the theoretical value of the isotopes in the ^{205}Au , ^{193}W and ^{193}Ta settings was shifted to the right of the corresponding peak. The second method was a better fit for these settings. For the ^{190}Lu setting, the first method aligned better. Both methods were compatible, but the second method was a better fit for most settings and was used in the plots shown throughout this thesis. The resulting ID Plots are shown in figures 5.21 to 5.24. Because the ^{193}W setting was used for the identification of all other isotopes it was cleaned of charge states and contamination at the cost of approximately half of its statistics. After applying the one by one [0,0] charge state selection (black circles in figure 5.5)), LISE++ simulation gates (e.g. red lines in 5.7) were used. Figure 5.20 shows how contamination of Au isotopes by Hg isotopes are removed using the strict LISE++ gate (red line in 5.7b)). Fragmentation of ^{208}Pb leaves $N = 126$; any production of $N = 127$ isotopes requires a charge-pickup reaction. While this mechanism is relevant at intermediate energies (e.g. [67]), at GSI energies above ~ 300 MeV/nucl. it is suppressed. Instead, charge-exchange via Delta-excitation dominates ([68, 69], explaining the observed presence of ^{206}Au ($N = 127$), while the chance for double exchange to ^{207}Au ($N = 128$) remains negligibly small.

Once the assignment of the peaks was concluded, each isotope was individually selected and counted. For each selected atomic number, the mass-to-charge ratios of its isotopes were plotted against their horizontal positions in the final focal plane, F4. The isotopes were selected one by one with cuts and counted. For the purpose of pure identification and counting of new isotopes, the removal of charge states and contamination was prioritized. This meant that the cuts were strict at the risk of reducing statistics. The charge was selected using the tight [0,0] state selection (red selection in 5.5) in combination with the boomerang selection of each charge, as shown in 5.6. The cuts used to count Pt isotopes in the ^{193}W setting are seen in Figure 5.25

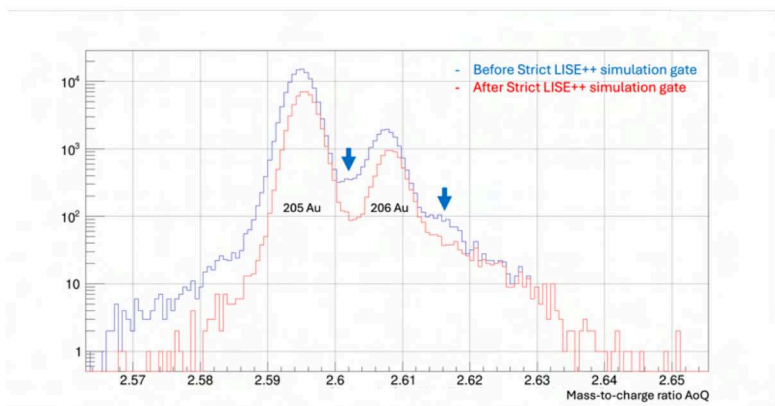


Figure 5.20: Mass-to-charge ratio AoQ of Au isotopes in the ^{193}W setting before and after applying the strict LISE++ gates. The blue arrows indicate the contamination.

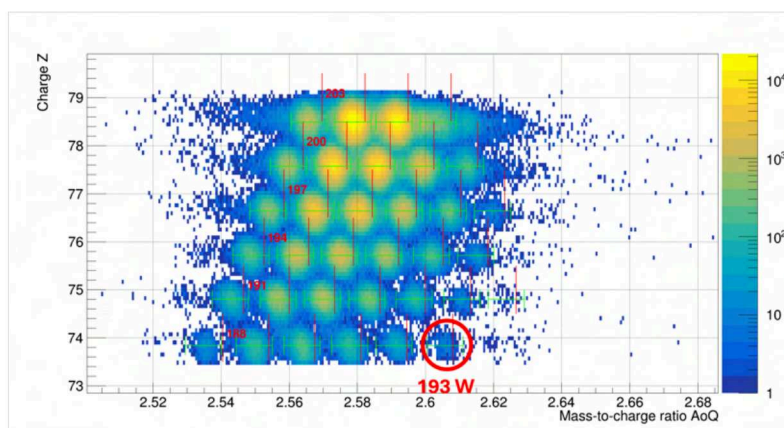


Figure 5.21: ID plot for the ^{205}Au setting. ^{193}W was anchored to its theoretical value in the ^{193}W setting. ^{193}W in this setting is encircled in red. AoQ values were shifted accordingly for all other settings. The theoretical values for AoQ, indicated by red lines, are shifted to the right relative to the data, but remain within the range of the corresponding isotope peaks, which are marked by green horizontal range bars.

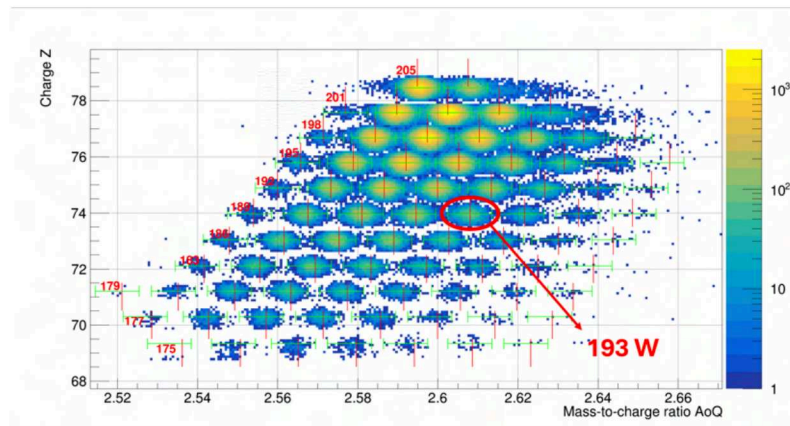


Figure 5.22: ID plot for the ^{193}W setting. ^{193}W , encircled in red, was anchored to its theoretical value in this setting. The theoretical values for all AoQ, indicated by red lines, are compatible with the data. The range of the corresponding isotope peaks are marked by green horizontal range bars.

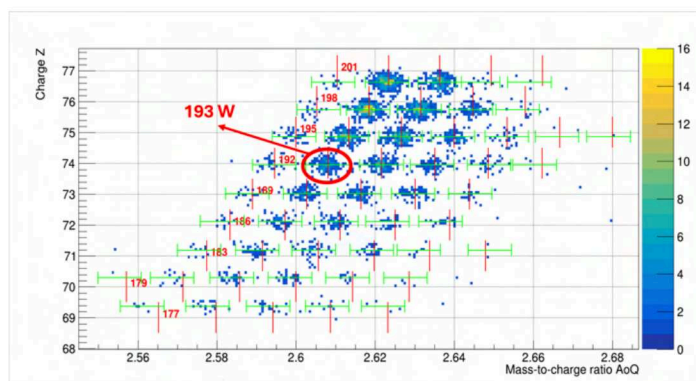


Figure 5.23: ID plot for the ^{193}Ta setting. ^{193}W was anchored to its theoretical value in the ^{193}W setting. ^{193}W in this setting is encircled in red. AoQ values were shifted accordingly for all other settings. The theoretical values for all AoQ, indicated by red lines, are compatible with the data. The range of the corresponding isotope peaks are marked by green horizontal range bars.

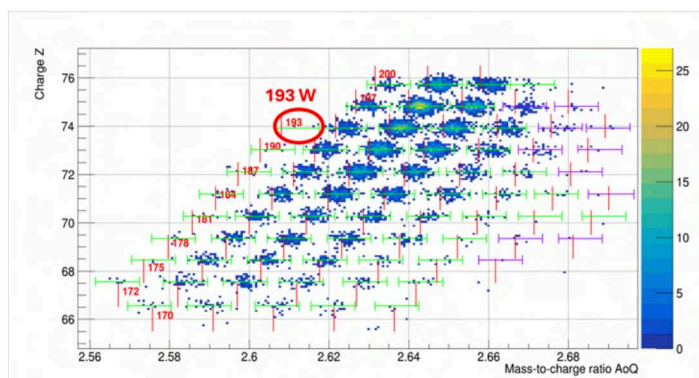


Figure 5.24: ID plot for the ^{193}Lu setting. ^{193}W was anchored to its theoretical value in the ^{193}W setting. ^{193}W in this setting is encircled in red. AoQ values were shifted accordingly for all other settings. The theoretical values for AoQ, indicated by red lines, are shifted to the left relative to the data, but remain within the range of the corresponding isotope peaks, which are marked by green horizontal range bars, purple range bars indicate the peaks of new isotopes.

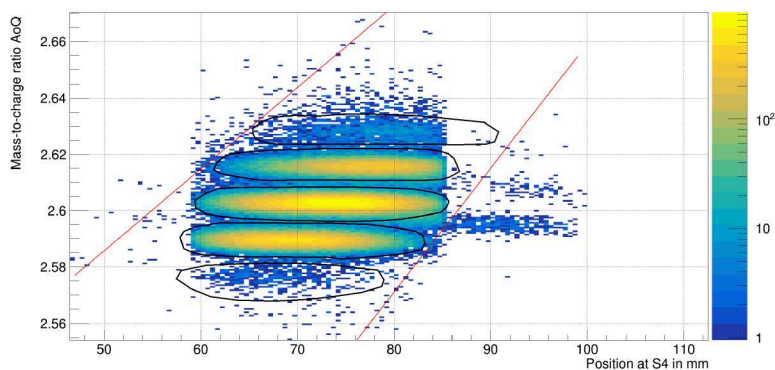


Figure 5.25: The cuts used to count Pt isotopes in the ^{193}W setting drawn in black. The red lines are the LISE++ simulations showing the left and right side edges of the position distributions of the Pt isotopes

6 Results and Discussion

In this chapter, the results of the experiment S468, carried out during FAIR Phase 0 at the GSI Fragment Separator (FRS), are presented, focusing on the identification of neutron-rich isotopes in the region close to the neutron number $N = 126$. The isotopes were measured across four different magnetic rigidity settings, with the FRS centered on ^{205}Au , ^{193}W , ^{193}Ta , and ^{190}Lu . For each setting, the isotopes were unambiguously identified, and their individual counts were determined. The identification rates achieved at the FRS will be presented, demonstrating the facility's capability to access nuclei in this challenging region.

As will be discussed in the following five isotopes measured during the ^{190}Lu setting were identified for the first time. Among them is ^{201}Re , a particularly significant discovery as it lies directly on the $N = 126$ line, marking a critical point in the r-process path and providing valuable input for nuclear structure and astrophysical models. Beyond the first observation of these nuclides, the analysis confirms the existence of seven neutron-rich isotopes recently reported by [70, 71].

6.1 Production and Identification in the Au Setting

The first fragment setting was centered on ^{205}Au . For this setting, the primary beam ^{208}Pb of 1.05 GeV/nucl., with an intensity of 4×10^8 ions/spill and a spill length of 1 second at a repetition rate of 3 seconds was used. The magnetic rigidity of the FRS was set at 12.538 Tm in the first and to 10.7348 Tm in the second half of the FRS. Data were recorded in this setting for approximately six hours. The isotopes were assigned in the resulting ID plots after all calibration and correction procedures, as well as the background and charge state suppression gates as explained in Chapter 5 were applied. The isotopes identified during the ^{205}Au setting and their counts are presented in Figure 6.1. The counting procedure is explained in Section 5.4. Because of the unknown effect of the burns in the

scintillators on the efficiencies and the restrictive cuts used to eliminate contamination for each isotope in combination with using an F4-only trigger, it is not possible to deduce cross sections from these counts.

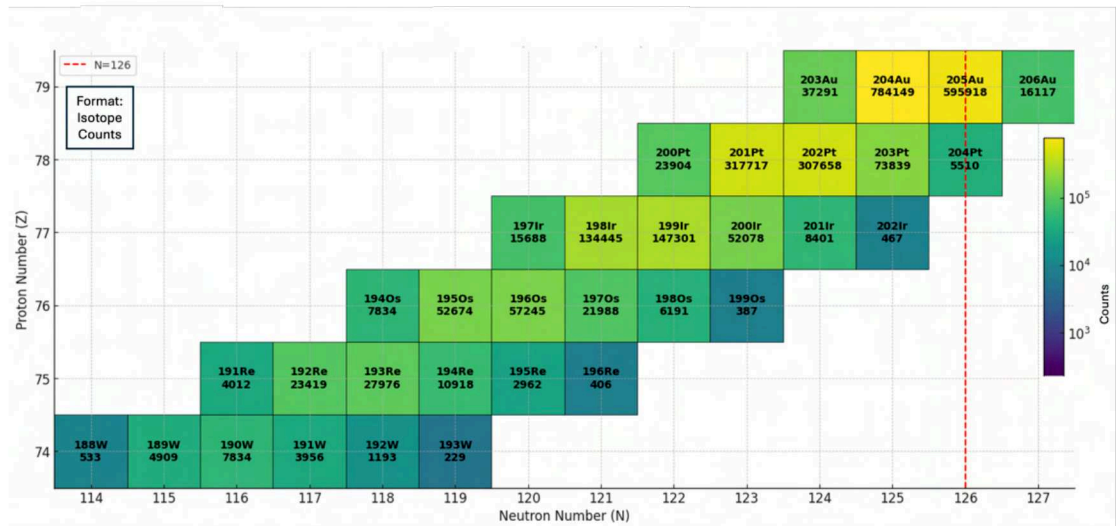


Figure 6.1: The isotopes identified during the ²⁰⁵Au setting are shown in the nuclear chart. They are labeled with their mass number and element symbol. The number below the element name indicates the total number of counts of the identified isotope. The dashed red line marks the neutron shell closure at $N = 126$. The duration of the measurement was approximately six hours.

In Figure 6.2a) the ID plot of the ²⁰⁵Au setting is shown after applying all the calibration, correction, charge state selections, and background filtering gates explained in Chapter 5, with the exception of the individual cuts for each isotope used to remove the remaining contamination and count the identified isotopes. As described in Section 5.4, this contamination was visible in the AoQ versus F4 position plots for each selected atomic number and was removed using individual cuts for each isotope. The resulting ID plot of all the unambiguously identified and counted isotopes, after the individual cuts are applied is shown in Figure 6.2b).

The isotopes produced during this setting are well known, providing a means to verify the identification. At the final focal plane of the FRS, the isotopes were implanted in the FRS-Ion Catcher for mass measurements. The analysis and the results of this measurement are described in [57].

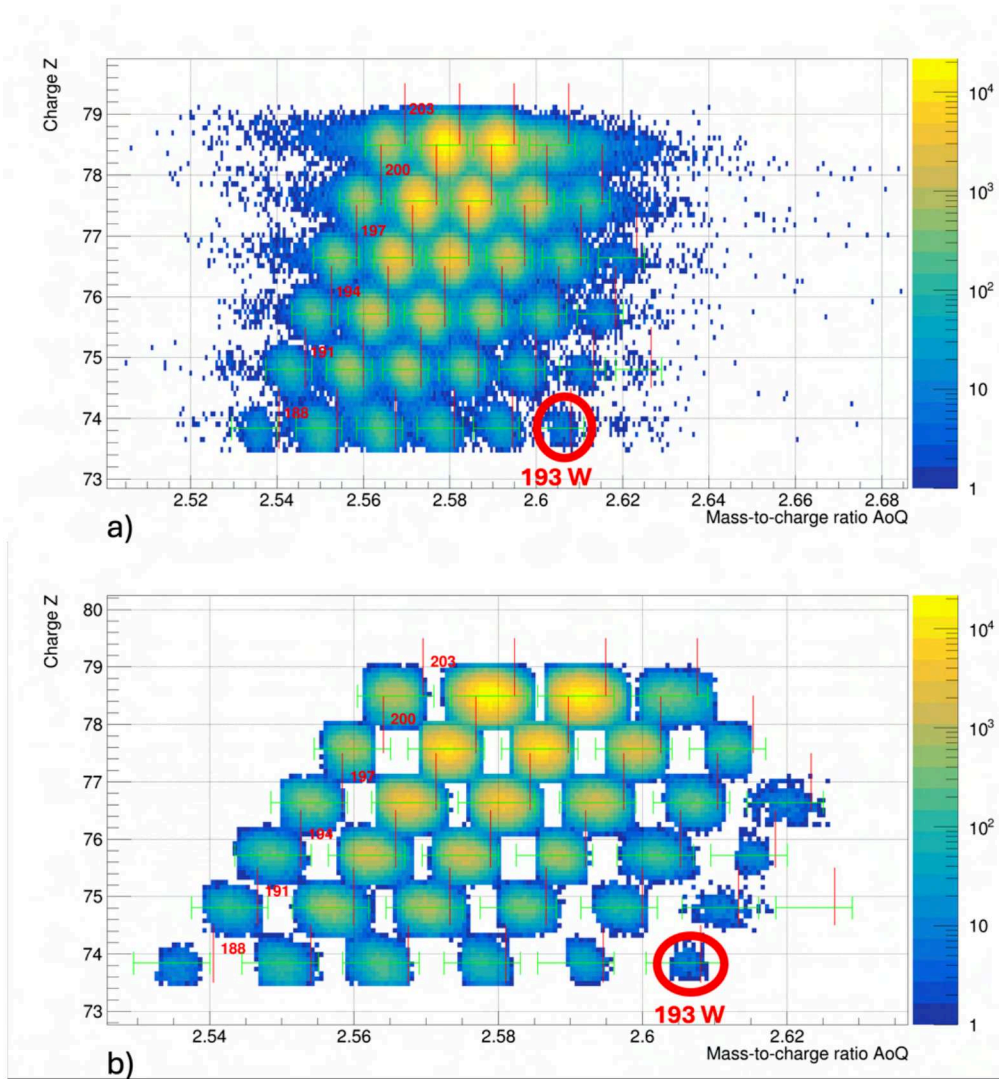


Figure 6.2: Final ID-Plots for the ^{205}Au setting: a) ID Plot with all the corrections, calibrations, charge state selections and background filtering before the individual cuts used for the counting of isotopes. b) ID-Plot after the individual counting cuts removing the remaining contamination were applied.

6.2 Production and Identification in the W Setting

The primary beam ^{208}Pb of 1.05 GeV/nucl., at an intensity of 4×10^8 ions/spill was used again for the ^{193}W setting. This time spill length consisted of 3 seconds at a repetition rate of 5 seconds. The magnetic rigidity of the FRS was set at 12.6853 Tm in the first section and at 11.0201 Tm in the second FRS section. The measurement lasted approximately 13 hours. The isotopes were assigned to the resulting ID plots, after all calibration and correction procedures were performed, as well as the background and charge state suppression gates as explained in Chapter 5. The isotopes identified during the ^{193}W setting and their counts are presented in Figure 6.3. The ^{193}W setting was used to anchor the AoQ values in all four settings. In particular, to compare and verify the identification in each setting. The assignment of isotopes and the counting procedure leading to identifications is explained in Section 5.4.

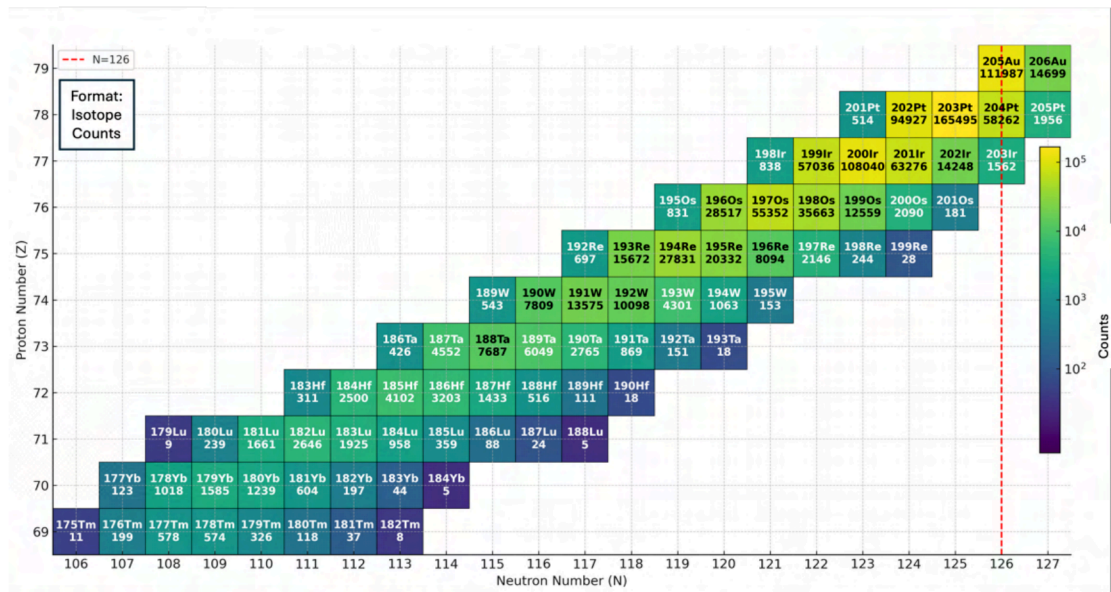


Figure 6.3: The isotopes identified during the ^{193}W setting are shown in the nuclear chart. They are labeled with their mass number and element symbol. The number below the element name indicates the total number of counts of the identified isotope. The dashed red line marks the neutron shell closure at $N = 126$. The duration of the measurement was approximately 13 hours.

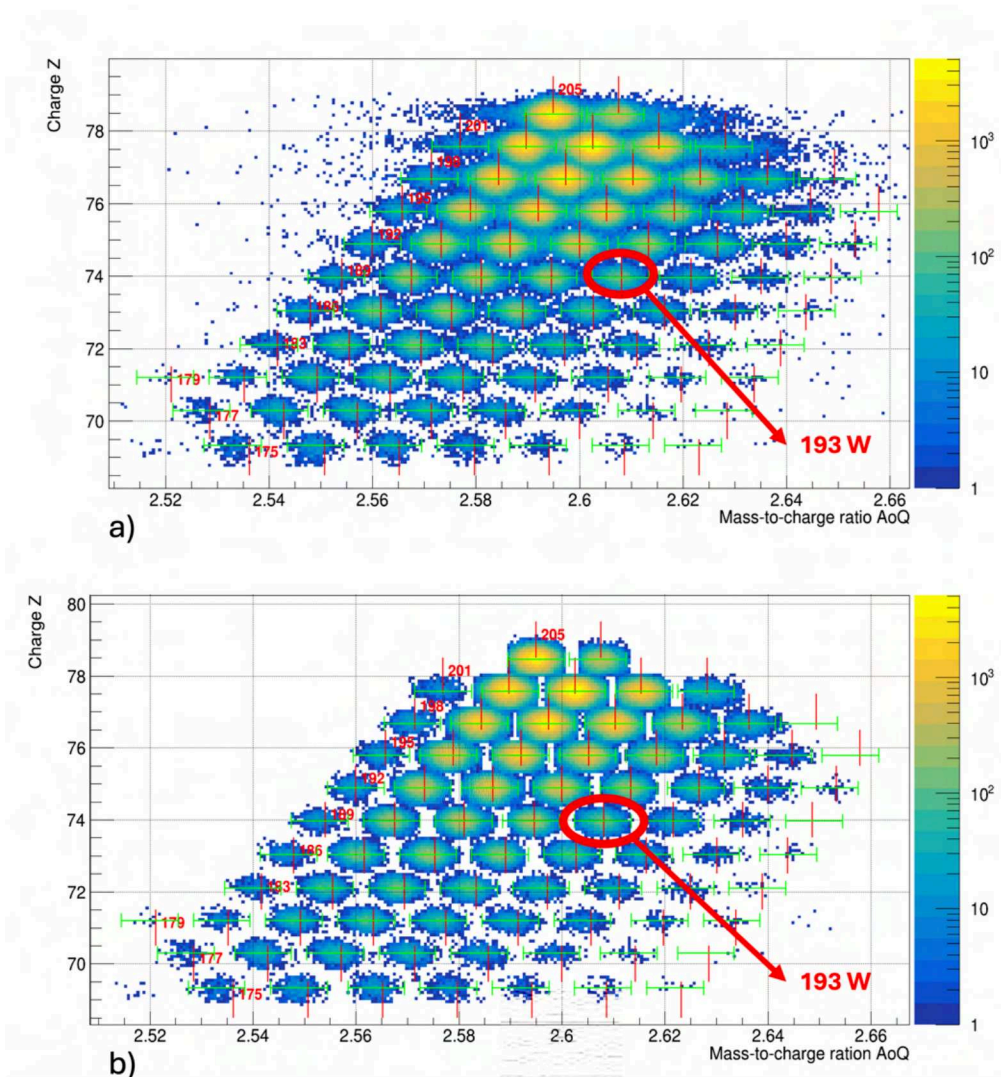


Figure 6.4: Final ID-Plots for the ^{193}W setting: a) ID Plot with all the corrections, calibrations, charge state selections and background filtering before the individual cuts used for the counting of isotopes. b) ID-Plot after the individual counting cuts removing the remaining contamination were applied.

As in the ^{205}Au setting, it is not possible to calculate the cross section using this counting procedure. The calculation of cross section for this setting (and the other main settings of this experiment) is challenging because of the unknown effect of the burns in the scintillators on the efficiencies and the restrictive cuts used to eliminate contamination for each isotope.

In Figure 6.4a) the ID plot of the ^{193}W setting is shown after applying all the calibration, correction, charge state selections, and background filtering gates explained in Chapter 5, with the exception of the individual cuts for each isotope used to remove the remaining contamination and count the identified isotopes. As described in Section 5.4, this contamination was visible in the AoQ versus F4 position plots for each selected atomic number and was removed using individual cuts for each isotope. The resulting ID plot of all the unambiguously identified and counted isotopes, after applying the individual cuts, is shown in Figure 6.4b).

Similarly to the ^{205}Au setting, the isotopes produced during this setting are well known, providing a means to verify the identification. Furthermore, the isotopes produced in this setting were implanted in the FRS Ion Catcher for mass measurements.

The ^{193}W setting was later used again for implantation in the active stopper for beta decay measurements. The spill length spill length was extended to 10 seconds to protect the active stopper detectors.

6.3 Production and Identification in the Ta Setting

The primary beam ^{208}Pb of 1.05 GeV/nucl., at an intensity of 1.5×10^9 ions/spill was used for the ^{193}Ta setting. The spill length consisted of 1 seconds at a repetition rate of 3 seconds. The magnetic rigidity of the FRS was set at 12.904 Tm in the first section and at 11.2702 Tm in the second FRS section. The measurement lasted approximately 2.5 hours. The isotopes were assigned to the resulting ID plots, after all calibration and correction procedures were performed, as well as the background and charge state suppression gates as explained in Chapter 5. The isotopes identified during the ^{193}Ta setting and their counts are presented in Figure 6.5. The assignment of isotopes and the counting procedure leading to identifications is explained in Section 5.4. The calculation of cross sections is not possible using this counting procedure, because of the restrictive selections that were used. In addition the effect of the burns in the plastic on the efficiencies have to be investigated and understood. Without independent information on the detection

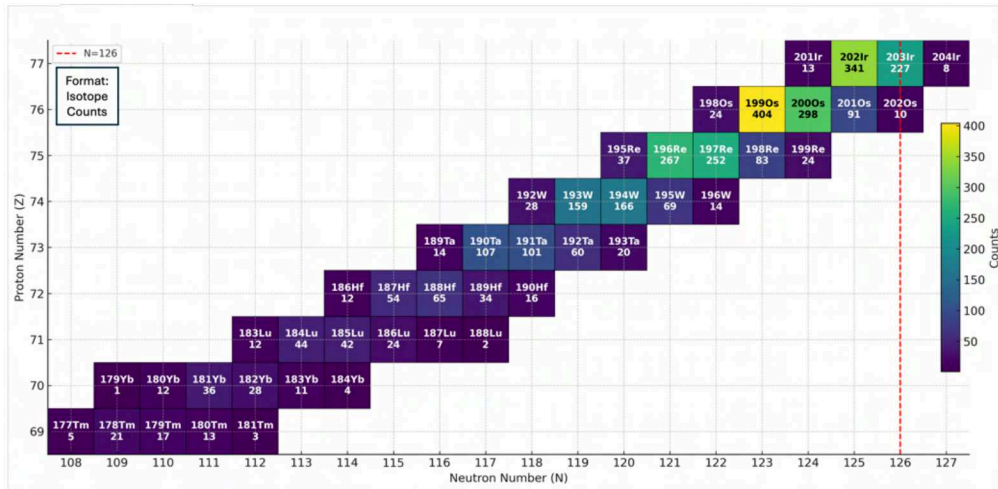


Figure 6.5: The isotopes identified during the ^{193}Ta setting are shown in the nuclear chart. They are labeled with their mass number and element symbol. The number below the element name indicates the total number of counts of the identified isotope. The dashed red line marks the neutron shell closure at $N = 126$. The duration of the measurement was approximately 2.5 hours.

probabilities of the plastic detectors at F2 and F4 using a combined trigger, such an endeavor is very challenging and related to significant uncertainties.

In Figure 6.6a) the ID plot of the ^{193}Ta setting is shown after applying all the calibration, correction, charge state selections, and background filtering gates explained in Chapter 5, with the exception of the individual cuts for each isotope used to remove the remaining contamination and count the identified isotopes. As described in Section 5.4, this contamination was visible in the AoQ versus F4 position plots for each selected atomic number and was removed using individual cuts for each isotope. The resulting ID plot of all the unambiguously identified and counted isotopes, after applying the individual cuts, is shown in Figure 6.6b).

There are no new isotopes in the ^{193}Ta setting, however this region contains isotopes with unknown beta-decays. For this setting the active stopper was installed at the final focal plane. The isotopes were implanted in the active stopper for beta decay measurements. The analysis of the beta decay was started prior to this work as part of the dissertation of Minna Luoma [58] and the author of this dissertation. Although first beta-decay life times were extracted, the results need to be validated after adapting the particle identification.

This topic will be discussed in more detail in Chapter 7.

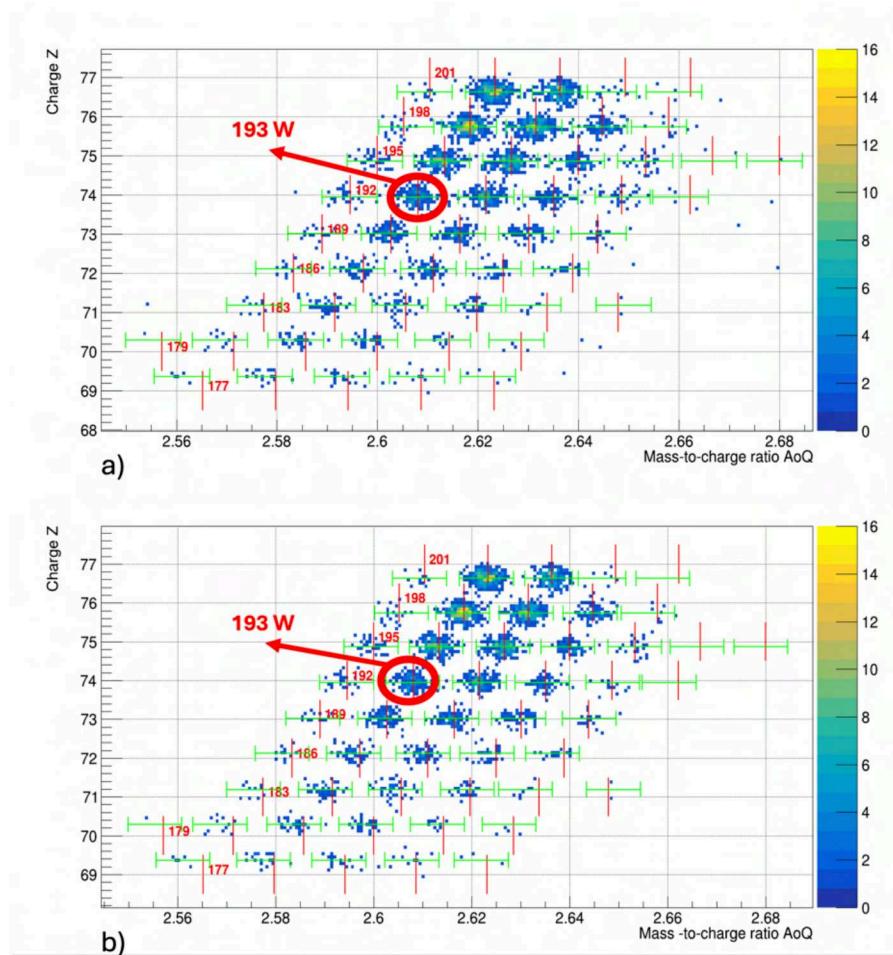


Figure 6.6: Final ID-Plots for the ^{193}Ta setting: a) ID Plot with all the corrections, calibrations, charge state selections and background filtering before the individual cuts used for the counting of isotopes. b) ID-Plot after the individual counting cuts removing the remaining contamination were applied.

6.4 Production and Identification in the Lu Setting

The primary beam ^{208}Pb of 1.05 GeV/u, at an intensity of 1.5×10^9 Hz was used for the ^{190}Lu setting. The spill length consisted of 0.7 seconds at a repetition rate of 3 seconds. The magnetic rigidity of the FRS was set at 13.117 Tm in the first section and at 11.529 Tm in the second FRS section. The measurement lasted approximately 2.5 hours. The isotopes were assigned to the resulting ID plots, after all calibration and correction procedures were performed, as well as the background and charge state suppression gates as explained in Chapter 5. The isotopes identified during the ^{190}Lu setting and their counts are presented in Figure 6.7. The assignment of isotopes and the counting procedure leading to identifications is explained in Section 5.4.

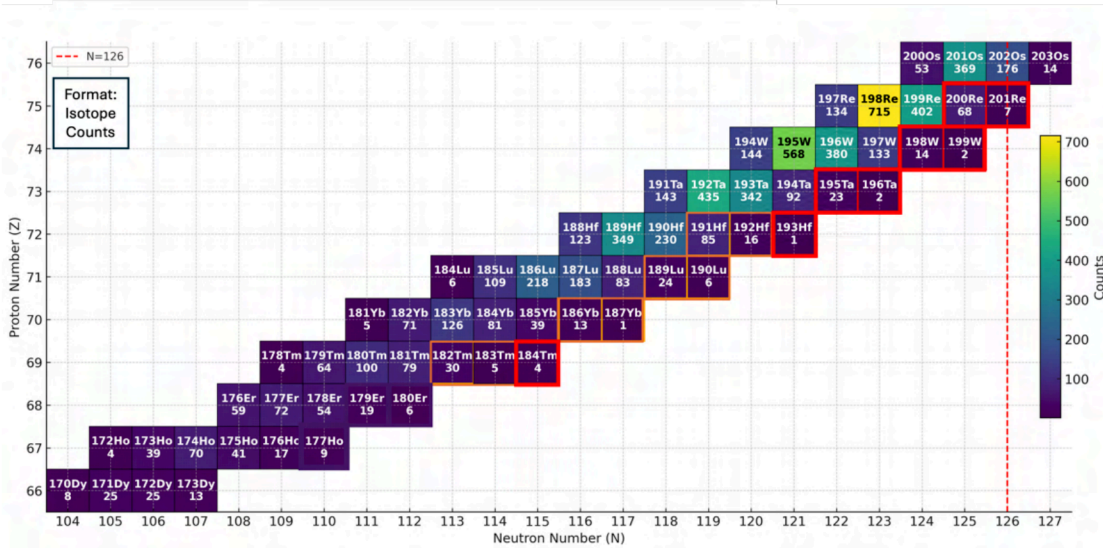


Figure 6.7: The isotopes identified during the ^{190}Lu setting are shown in the nuclear chart. They are labeled with their mass number and element symbol. The number below the element name indicates the total number of counts of the identified isotope. The dashed red line marks the neutron shell closure at $N = 126$. The duration of the measurement was approximately 42.5 hours. New isotopes observed during this setting are indicated in with red. Orange outlines show isotopes that were discovered in 2023 [70] and 2024 [71] after the beam time of the S468 experiment.

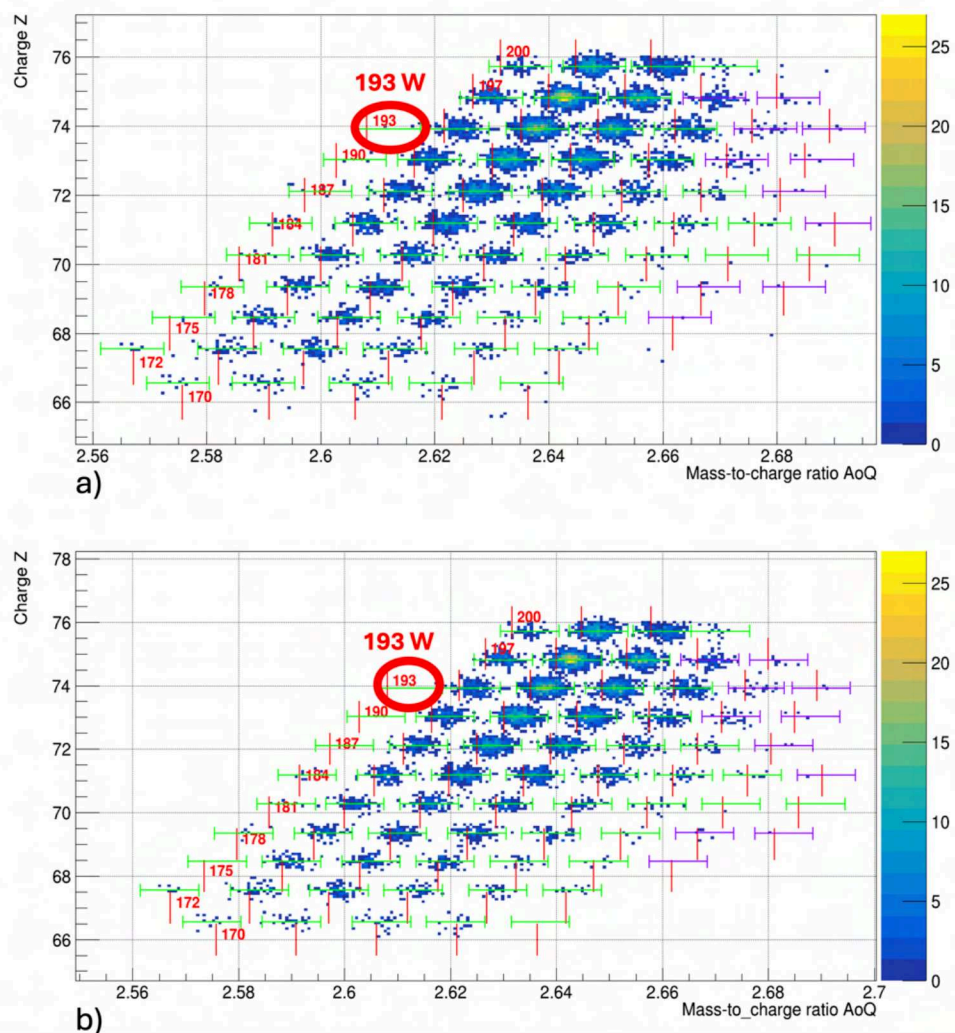


Figure 6.8: Final ID-Plots for the ^{190}Lu setting: a) ID Plot with all the corrections, calibrations, charge state selections and background filtering before the individual cuts used for the counting of isotopes. b) ID-Plot after the individual counting cuts removing the remaining contamination were applied.

In Figure 6.8a) the ID plot of the ^{190}Lu setting is shown after applying all the calibration, correction, charge state selections, and background filtering gates explained in Chapter 5, with the exception of the individual cuts for each isotope used to remove the remaining contamination and count the identified isotopes. As described in Section 5.4, this contamination was visible in the AoQ versus F4 position plots for each selected atomic number and was removed using individual cuts for each isotope. The resulting ID plot of all the unambiguously identified and counted isotopes, after applying the individual cuts, is shown in Figure 6.8b).

New isotopes were observed in the ^{190}Lu setting. They are indicated in Figure 6.7 in red (the threshold to claim the discovery of nuclei is 3 reliable counts. This is applied for instance in [71]). The experiment was carried out in April 2020. Since then new isotopes in this region were discovered by [70] and [71]. Their existence was confirmed in this experiment with the exception of ^{187}Yb that had only one event. The number of event of the isotopes discovered in [71] compared to the counts of the same isotopes in this setting are shown in Table 6.1

	^{182}Tm counts	^{183}Tm counts	^{186}Yb counts	^{187}Yb counts	^{190}Lu counts
2024 discovery	29	7	27	3	5
confirmed in S468	30	5	13	1	6

Table 6.1: Comparison of the counts of the isotopes during in the first discovery in 2024 [71] and the S468 experiment.

The new isotopes discovered in the S468 experiment will be presented in section 6.5. In addition to the new isotopes, this region contains isotopes with unknown beta-decays. The active stopper was installed at the final focal plane for beta-decay measurements.

6.5 New Isotopes

The central achievement of this work is the identification of several previously unobserved neutron-rich isotopes near the magic neutron number $N = 126$, a region of great interest for both nuclear structure studies and astrophysical nucleosynthesis models. The production and separation of the isotopes is described in Chapter 4. The data analysis leading to the identification is explained in detail in Chapter 5. Among the newly identified nuclei

are five isotopes discovered during the setting centered on ^{190}Lu , including the particularly significant ^{201}Re , which lies directly on the $N = 126$ shell closure. In the following sections, the measured isotope yields for these isotopes will be presented. In particular, the impact of the background suppression gates on the yields of the new isotopes will be discussed.

Figure 6.9 shows the number of counts for each isotope that was identified for the first time. The isotopes were counted using different combinations of gates. The different gates and their general effect on each settings production yields is discussed in Chapter 5. The gates referred to as Y2 in Figure 6.9 set on the vertical position of the event measured at F2. The *Csum* gates are checking the control sum of both TPCs at F2. The third gate, *SCvsTpc*, selects events in which the horizontal position at F2 measured by the TPCs matches the prediction from the scintillators. While for the settings with higher rates at F2, ^{205}Au and ^{193}W all gates had significant impact on the separability of the individual isotopes. For the lower statistic settings, ^{193}Ta and in particular ^{190}Lu no improvement of the separability or resolution after applying the *Csum* or *SCvsTpc* gates were observed.

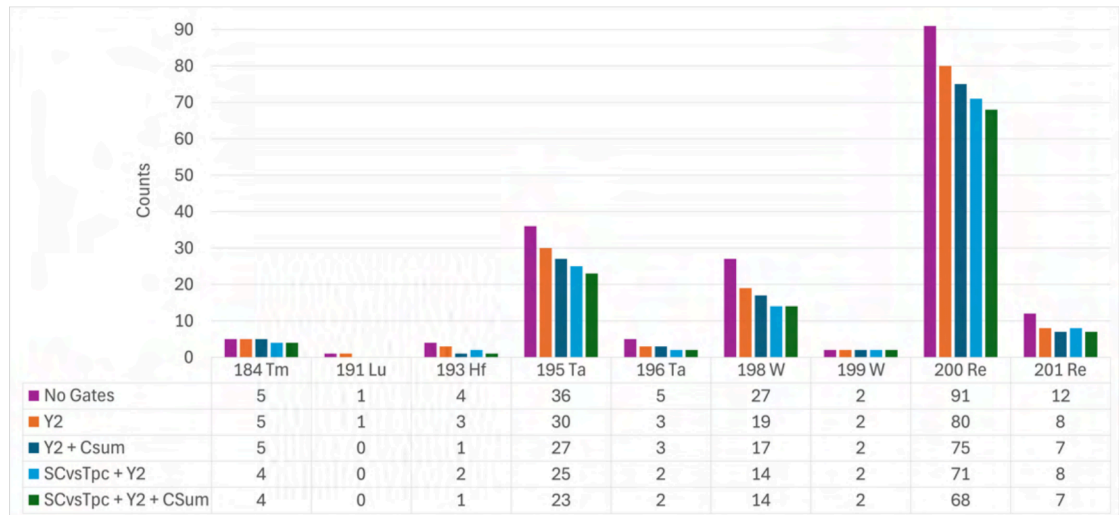


Figure 6.9: Number of counts of observed new isotopes for different gate combinations.

In total, events that were compatible with nine new isotopes were observed. In previous publications of new isotope discoveries –in [70] and [71]– observations of three events compatible with the isotope were considered sufficient to claim the discovery of a new isotope. With the additional requirement of minimum three events seven new isotopes are

observed when the Y2 gates are applied. Out of these seven five remain, when all gates are applied: ^{184}Tm (4 events), ^{195}Ta (23 events), ^{198}W (14 events), ^{200}Re (68 events) and the $N = 126$ isotope ^{201}Re (7 events).

The cuts used to select and count the individual isotopes are shown in figures 6.10 to 6.13. Their F4 positions are centered/more to the left compared to the expected position distributions predicted by LISE++. This excludes the possibility of contamination, that is expected on the right side.

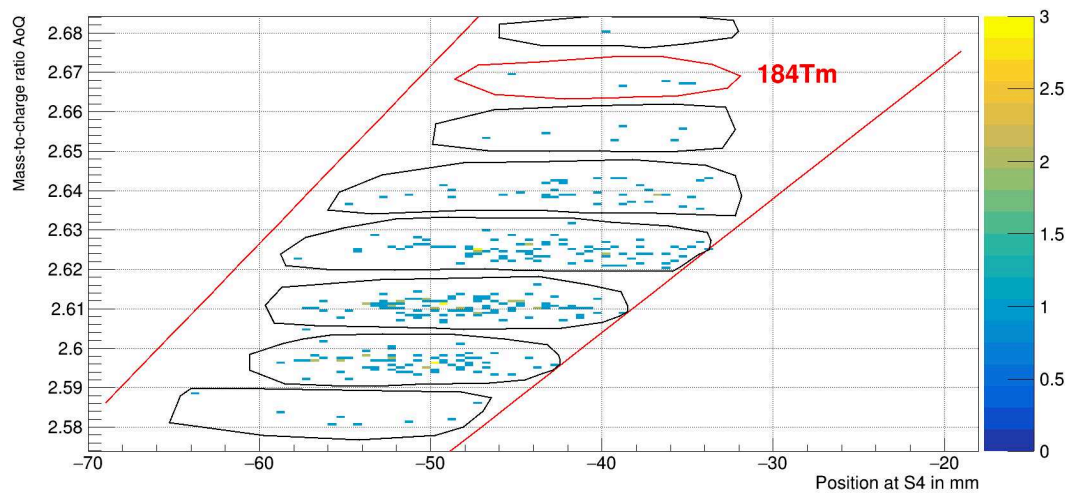


Figure 6.10: The cuts used for selecting Tm isotopes. The red lines show the edges of the position distributions according to LISE. The cuts for the new isotopes are shown in red.

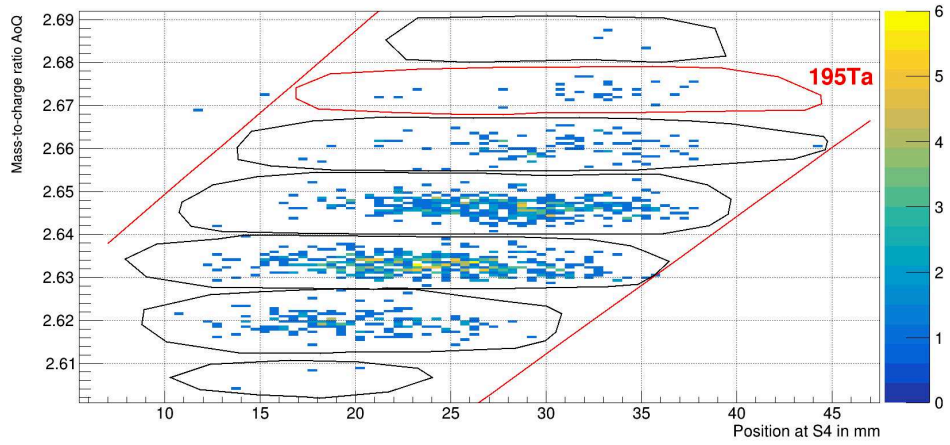


Figure 6.11: The cuts used for selecting Ta isotopes. The red lines show the edges of the position distributions according to LISE. The cuts for the new isotopes are shown in red.

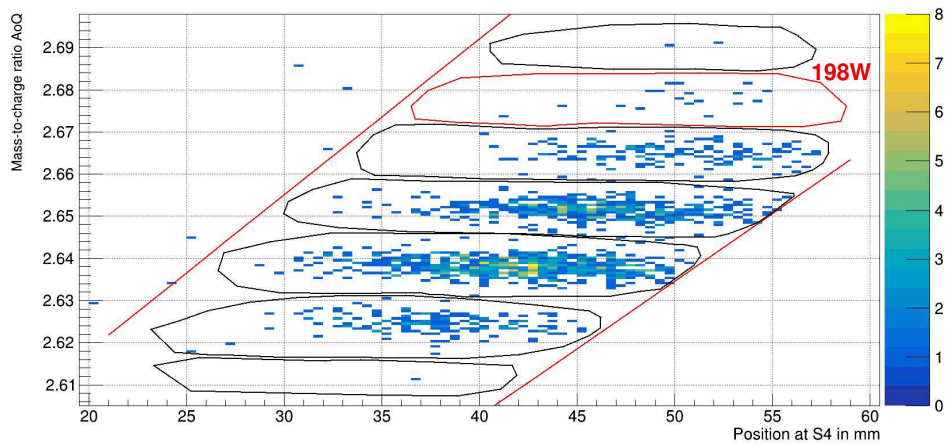


Figure 6.12: The cuts used for selecting W isotopes. The red lines show the edges of the position distributions according to LISE. The cuts for the new isotopes are shown in red.

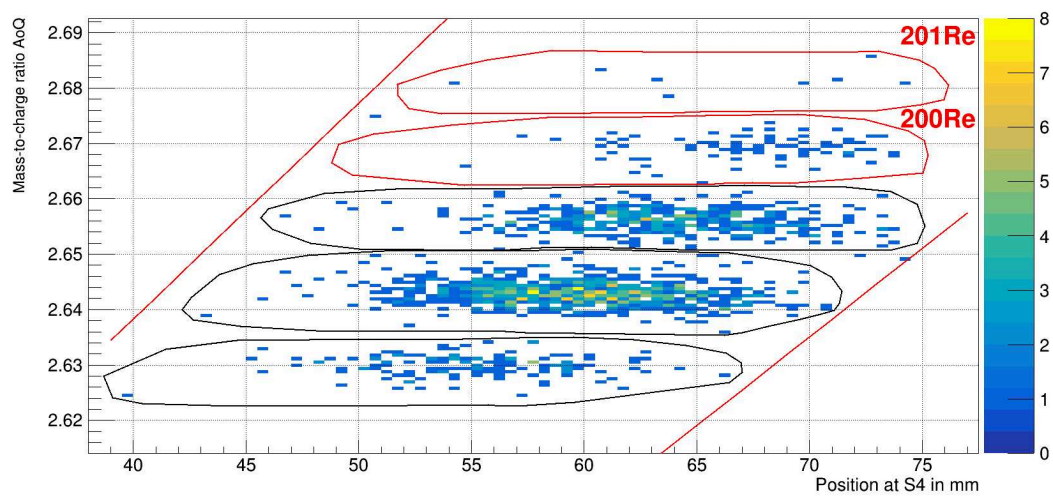


Figure 6.13: The cuts used for selecting Re isotopes. The red lines show the edges of the position distributions according to LISE. The cuts for the new isotopes are shown in red.

7 Perspectives for Continued Research on the S468 Data

The data collected in this experiment offer significant potential beyond the initial identification of isotopes. A considerable number of nuclei were produced in regions where masses, beta-decay properties, and/or cross sections are still unknown. Data analysis for masses is described in [57].

In this chapter, the potential for beta-decay and cross-section analysis will be discussed.

7.1 Cross Section of Nuclei Close to $N = 126$

The isotopes produced during the four main settings ^{205}Au , ^{193}W , ^{193}Ta and ^{190}Lu are shown in Figure 7.1. It is a relatively unexplored region close to the neutron magic number $N = 126$. Measurement of production cross sections in this region is of key importance not only to improve r-process nucleosynthesis models, but also to demonstrate the capabilities of the GSI fragment separator (FRS) to access neutron-rich nuclei near $N = 126$. The observed yields in this relatively unexplored region highlight the strong potential of the FRS for future experimental campaigns and serve as a valuable reference for the planning and optimization of upcoming experiments targeting even more exotic isotopes.

The data set provided by this experiment offers the possibility to determine production cross sections in this region. The challenges facing this analysis include understanding the effects of burns in the scintillators at F2 and F4 on efficiency. Position dependencies are expected and need to be well understood. In addition a good understanding and estimation of the present contamination is crucial to avoid too restrictive selections while cleaning charge states.

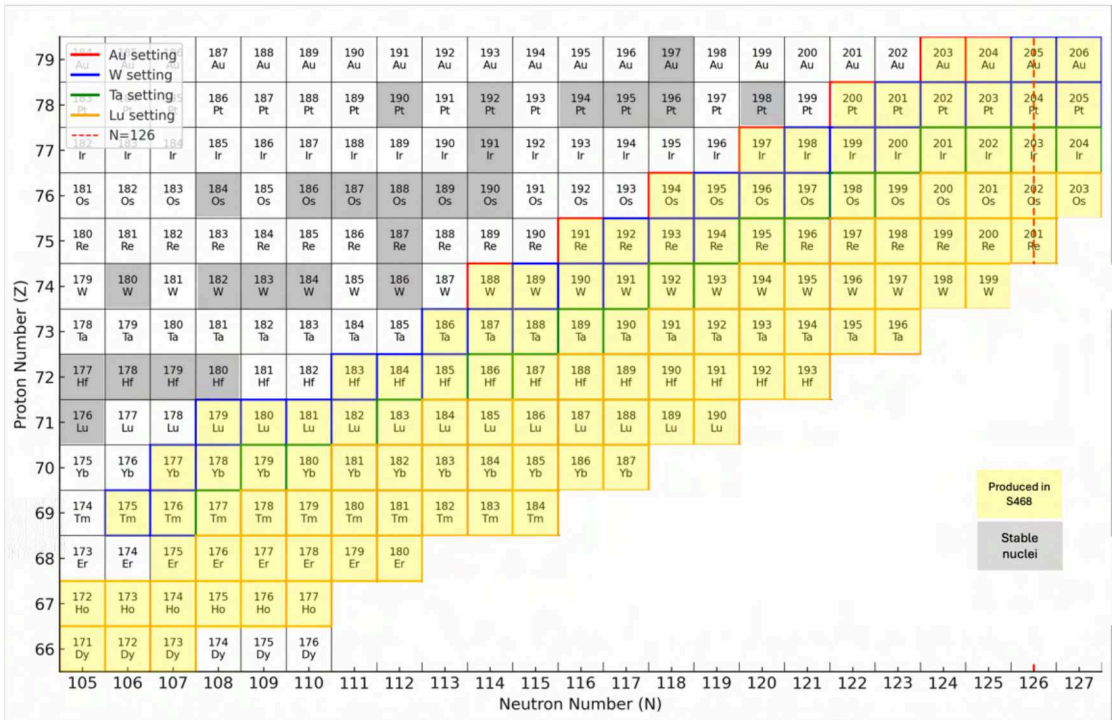


Figure 7.1: The combined isotopes produced across the four main setting centered on ^{205}Au , ^{193}W , ^{193}Ta , and ^{190}Lu during the S468 experiment.

7.2 Beta-decay of Nuclei Close to N = 126

For beta decay measurement, the isotopes were implanted in the active stopper, which was installed at F4 during the ^{193}Ta and ^{190}Lu settings. Based on the method applied by [72] for the beta-decay analysis of a similar FRS experiment, first attempts to extract beta-decay half-lives from the present data set have already been made. The method and the first results can be found in [58]. Figure 7.2 shows a schematized illustration of the method.

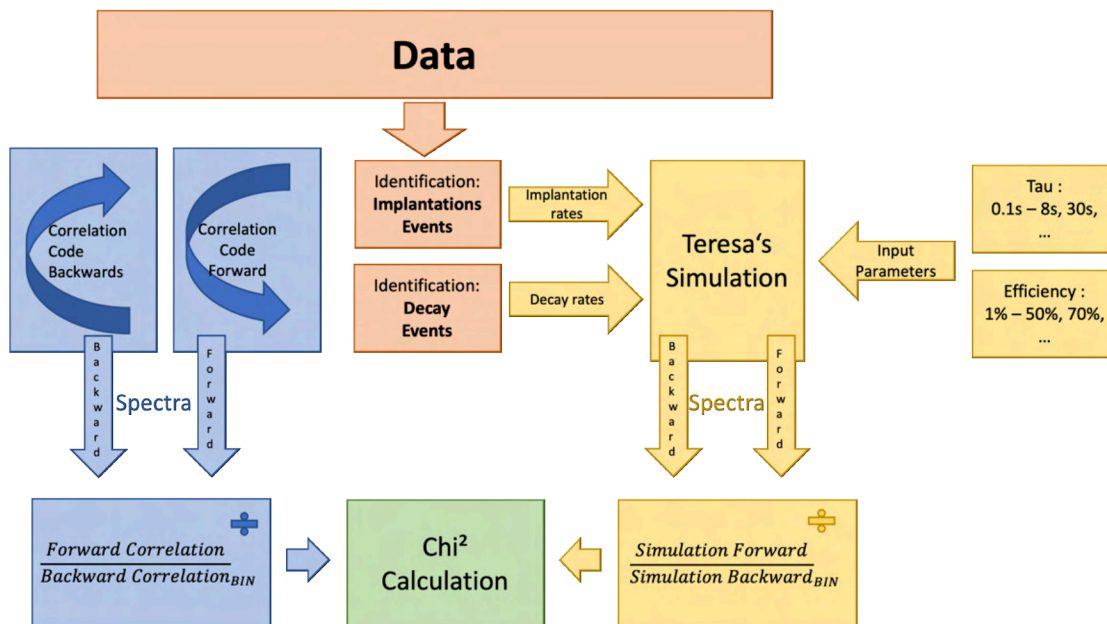


Figure 7.2: The method used to extract beta decay lifetimes from the data. As a first step, the rates of implantation and beta-decay are determined. Based on these rates, a simulation creates decay and background spectra for different lifetimes and detection efficiencies. The decay-to-background ratios are then compared to spectra from the actual data. With the help of χ^2 -calculations, the lifetime and efficiencies are extracted.

The first attempts to extract beta decay lifetimes were faced with challenges. Noise in the active stopper caused primarily by light fission fragments complicated the identification of beta-decay events. For this reason, it was crucial to reduce contamination in implantation

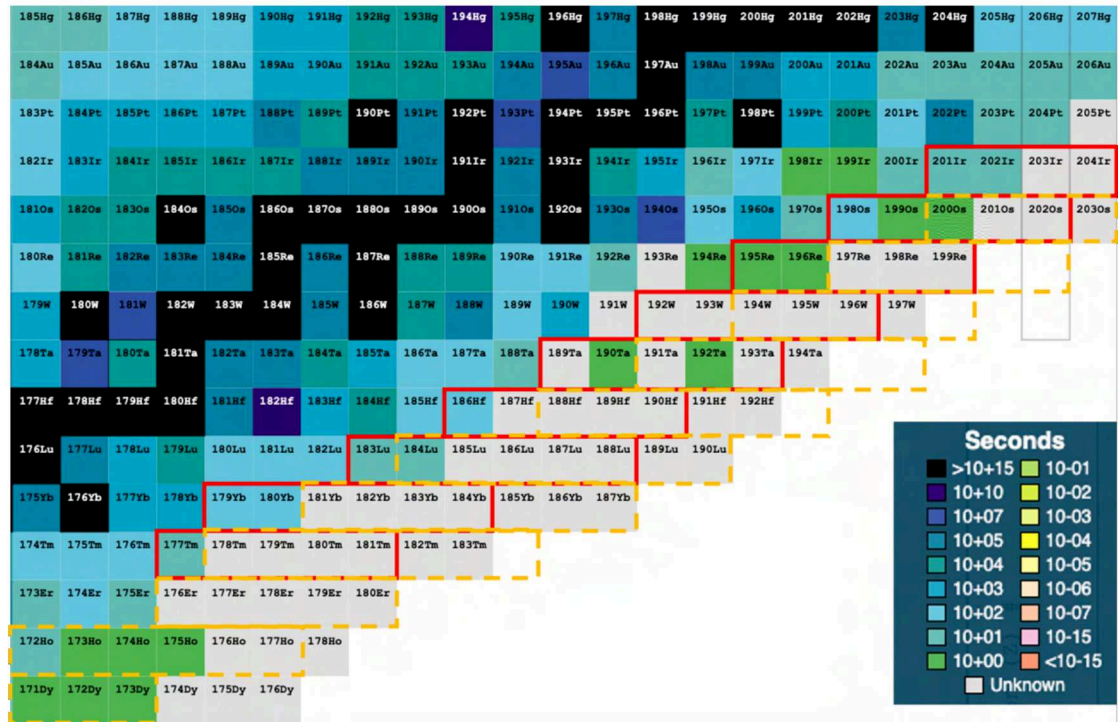


Figure 7.3: Beta-decay lifetimes from [14] in the region of production of the ^{193}Ta and ^{190}Lu settings. Isotopes with unknown lifetimes are shown in gray.

rates. The first attempts of beta-decay analysis were based on a particle identification, in which significant contamination of the isotopes was still present, causing additional noise. Adapting existing codes to the new particle identification with significantly less contamination in implantation rates could help improve the results.

In figure 7.3 beta-decays in the production regions of the ^{193}Ta and ^{190}Lu settings is shown. The number of unknown isotopes is remarkable and a motivating factor to pursue with the beta-decay analysis.

8 Conclusion

In this work, the data analysis for particle identification in the S468 experiment conducted at the Fragment Separator (FRS) of GSI has been presented. The experiment successfully accessed a previously unexplored region of the nuclear chart, covering neutron-rich isotopes near the $N = 126$ shell closure. Due to the experimental challenges associated with producing these exotic nuclei, much of this region remains largely unknown, with many isotopes either undiscovered or lacking basic nuclear properties such as masses, half-lives, and production cross sections.

The central result of this work is the discovery of five new isotopes. The isotopes ^{184}Tm (4 events), ^{195}Ta (23 events), ^{198}W (14 events), ^{200}Re (68 events) and ^{201}Re (7 events)—an isotope located directly on the $N = 126$ line—were identified for the first time. These discoveries mark a significant contribution to the extension of the known nuclear landscape towards the r-process path. Furthermore, the existence of seven recently discovered isotopes [70, 71] were confirmed. Beyond the direct discoveries, the dataset obtained in this experiment offers promising potential for further analyses, particularly in the determination of new β -decay half-lives and production cross sections.

Overall, the results of this experiment demonstrate the high potential of the FRS at GSI for exploring the neutron-rich region around $N = 126$ and provide a strong foundation for future experimental and theoretical investigations in this critical area of nuclear physics.

Bibliography

- [1] Pierre Radvanyi and Jacques Villain. “The discovery of radioactivity”. In: *Comptes Rendus. Physique* 18.9-10 (2017), pp. 544–550. DOI: 10.1016/j.crhy.2017.10.008. URL: <https://www.sciencedirect.com/science/article/pii/S1631070517300786>.
- [2] E. Rutherford. “LXXIX. The scattering of α and β particles by matter and the structure of the atom”. In: *The London, Edinburgh, and Dublin Philosophical Magazine and Journal of Science* 21.125 (1911), pp. 669–688. ISSN: 1941-5982. DOI: 10.1080/14786440508637080. URL: <https://inspirehep.net/literature/45404>.
- [3] Orme Masson. “XXIV. The constitution of atoms”. In: *The London, Edinburgh, and Dublin Philosophical Magazine and Journal of Science* 41.242 (1921), pp. 281–285. ISSN: 1941-5982. DOI: 10.1080/14786442108636219.
- [4] James Chadwick. “The existence of a neutron”. In: *Proceedings of the Royal Society of London. Series A, Containing Papers of a Mathematical and Physical Character* 136.830 (1932), pp. 692–708. ISSN: 0950-1207. DOI: 10.1098/rspa.1932.0112.
- [5] A. S. Eddington. “The Internal Constitution of the Stars”. In: *The Scientific Monthly* 11.4 (1920), pp. 297–303. ISSN: 00963771. URL: <http://www.jstor.org/stable/6491>.
- [6] H. A. Bethe. “Energy Production in Stars”. In: *Physical Review* 55.5 (1939), pp. 434–456. ISSN: 0031-899X. DOI: 10.1103/PhysRev.55.434.
- [7] E. Margaret Burbidge et al. “Synthesis of the Elements in Stars”. In: *Reviews of Modern Physics* 29.4 (1957), pp. 547–650. ISSN: 0034-6861. DOI: 10.1103/RevModPhys.29.547.
- [8] K. Lodders, H. Palme, and H.-P. Gail. “4.4 Abundances of the elements in the Solar System”. In: vol. 4B, pp. 712–770. DOI: 10.1007/978-3-540-88055-4_34.

-
- [9] Martin Asplund et al. “The Chemical Composition of the Sun”. In: *Annual Review of Astronomy and Astrophysics* 47.1 (2009), pp. 481–522. ISSN: 0066-4146. DOI: 10.1146/annurev.astro.46.060407.145222. URL: <http://arxiv.org/pdf/0909.0948>.
- [10] John J. Cowan et al. “Origin of the heaviest elements: The rapid neutron-capture process”. In: *Reviews of Modern Physics* 93.1 (2021), p. 015002. ISSN: 0034-6861. DOI: 10.1103/RevModPhys.93.015002.
- [11] T. Kajino et al. “Current status of r -process nucleosynthesis”. In: *Progress in Particle and Nuclear Physics* 107 (2019), pp. 109–166. ISSN: 01466410. DOI: 10.1016/j.pnpnp.2019.02.008. URL: <http://arxiv.org/pdf/1906.05002>.
- [12] Daniel M. Siegel. “GW170817 –the first observed neutron star merger and its kilonova: Implications for the astrophysical site of the r-process”. In: *The European Physical Journal A* 55.11 (2019). ISSN: 1434-6001. DOI: 10.1140/epja/i2019-12888-9. URL: <http://arxiv.org/pdf/1901.09044>.
- [13] Daniel M. Siegel. “GW170817 –the first observed neutron star merger and its kilonova: Implications for the astrophysical site of the r-process”. In: *The European Physical Journal A* 55.11 (2019). ISSN: 1434-6001. DOI: 10.1140/epja/i2019-12888-9. URL: <http://arxiv.org/pdf/1901.09044>.
- [14] *NuDat 3*. 5/22/2025. URL: <https://www.nndc.bnl.gov/nudat3/>.
- [15] Christian Iliadis. *Nuclear Physics of Stars*. 1st ed. New York Academy of Sciences Series. Newark: John Wiley & Sons Incorporated, 2015. ISBN: 9783527336494. URL: <https://ebookcentral.proquest.com/lib/kxp/detail.action?docID=7104659>.
- [16] Richard H Cyburt et al. “Big bang nucleosynthesis: Present status”. In: *Reviews of Modern Physics* 88.1 (2016), p. 015004.
- [17] Franz Käppeler et al. “The s process: Nuclear physics, stellar models, and observations”. In: *Reviews of Modern Physics* 83.1 (2011), pp. 157–193.
- [18] Claudio Arlandini et al. “Neutron Capture in Low–Mass Asymptotic Giant Branch Stars: Cross Sections and Abundance Signatures”. In: *The Astrophysical Journal* 525.2 (1999), pp. 886–900. ISSN: 0004-637X. DOI: 10.1086/307938. URL: <https://iopscience.iop.org/article/10.1086/307938>.
- [19] H. Geissel et al. “The GSI projectile fragment separator (FRS): a versatile magnetic system for relativistic heavy ions”. In: *Nuclear Instruments and Methods in Physics Research Section B: Beam Interactions with Materials and Atoms* 70.1-4 (1992), pp. 286–297. ISSN: 0168583X. DOI: 10.1016/0168-583X(92)95944-M.

-
-
- [20] Ulli Köster et al. “(Im-) possible ISOL beams”. In: *The European Physical Journal Special Topics* 150 (2007), pp. 285–291.
- [21] Oleg Tarasov. *Production of Fast Rare Isotope Beams*. 2013. URL: https://lise.frib.msu.edu/paper/Euroschool2013/1_Introduction.pdf.
- [22] Gottfried Münzenberg. “The separation techniques for secondary beams”. In: *Nuclear Instruments and Methods in Physics Research Section B: Beam Interactions with Materials and Atoms* 70.1-4 (1992), pp. 265–275. ISSN: 0168583X. DOI: 10.1016/0168-583X(92)95942-K. URL: <https://www.sciencedirect.com/science/article/pii/0168583X9295942K>.
- [23] O Tarasov. “Analysis of momentum distributions of projectile fragmentation products”. In: *Nuclear Physics A* 734 (2004), pp. 536–540.
- [24] DJ Morrissey. “Systematics of momentum distributions from reactions with relativistic ions”. In: *Physical Review C* 39.2 (1989), p. 460.
- [25] Tohru Motobayashi. “World new facilities for radioactive isotope beams”. In: *EPJ Web of Conferences* 66 (2014), p. 01013. DOI: 10.1051/epjconf/20146601013.
- [26] R Anne et al. “The achromatic spectrometer LISE at GANIL”. In: *Nuclear Instruments and Methods in Physics Research Section A: Accelerators, Spectrometers, Detectors and Associated Equipment* 257.2 (1987), pp. 215–232.
- [27] T Kubo et al. “The RIKEN radioactive beam facility”. In: *Nuclear Instruments and Methods in Physics Research Section B: Beam Interactions with Materials and Atoms* 70.1-4 (1992), pp. 309–319.
- [28] D _ J Morrissey et al. “Commissioning the A1900 projectile fragment separator”. In: *Nuclear Instruments and Methods in Physics Research Section B: Beam Interactions with Materials and Atoms* 204 (2003), pp. 90–96.
- [29] Guo Zhongyan et al. “Experimental setup at RIBLL1”. In: *Chinese Physics C* 20.6 (1996), pp. 491–497.
- [30] Antonio CC Villari et al. “The accelerated ISOL technique and the SPIRAL project”. In: *Nuclear Physics A* 693.1-2 (2001), pp. 465–476.
- [31] Säid Essabaa et al. “The radioactive beam facility ALTO”. In: *Nuclear Instruments and Methods in Physics Research Section B: Beam Interactions with Materials and Atoms* 317 (2013), pp. 218–222.
- [32] J Dilling, R Krücken, and G Ball. “ISAC overview”. In: *Hyperfine Interactions* 225.1 (2014), pp. 1–8.

-
- [33] Dietrich Habs et al. “The rex-isolde project”. In: *Hyperfine interactions* 129 (2000), pp. 43–66.
- [34] PG Hansen and Björn Jonson. “The neutron halo of extremely neutron-rich nuclei”. In: *Europhysics Letters* 4.4 (1987), p. 409.
- [35] T Motobayashi et al. “Large deformation of the very neutron-rich nucleus ^{32}Mg from intermediate-energy Coulomb excitation”. In: *Physics Letters B* 346.1-2 (1995), pp. 9–14.
- [36] Akira Ozawa et al. “New magic number, $N=16$, near the neutron drip line”. In: *Physical review letters* 84.24 (2000), p. 5493.
- [37] B Bastin et al. “Collapse of the $n=28$ shell closure in ^{42}Si ”. In: *Physical review letters* 99.2 (2007), p. 022503.
- [38] Yasushige Yano and Tohru Motobayashi. “Radioactive isotope beam factory at RIKEN (RIBF)”. In: *Nuclear Physics News* 17.4 (2007), pp. 5–10.
- [39] Matthaeus Leitner et al. “The FRIB project at MSU”. In: *Proc. of the 16th Workshop on RF Superconductivity*. 2013, p. 1.
- [40] H. Geissel et al. “The Super-FRS project at GSI”. In: *Nuclear Instruments and Methods in Physics Research Section B: Beam Interactions with Materials and Atoms* 204 (2003). 14th International Conference on Electromagnetic Isotope Separators and Techniques Related to their Applications, pp. 71–85. ISSN: 0168-583X. DOI: [https://doi.org/10.1016/S0168-583X\(02\)01893-1](https://doi.org/10.1016/S0168-583X(02)01893-1). URL: <https://www.sciencedirect.com/science/article/pii/S0168583X02018931>.
- [41] *Accelerator Facility*. URL: https://www.gsi.de/en/researchaccelerators/accelerator_facility.
- [42] P Spädtke et al. “Ion source development at GSI”. en. In: *Rev. Sci. Instrum.* 69.2 (Feb. 1998), pp. 1079–1081.
- [43] O Bohne. “Status Report on the Unilac”. In: *IEEE Trans. Nucl. Sci.* 24.3 (June 1977), pp. 1070–1075.
- [44] L Groening et al. *UNILAC Status Report*. 2014.
- [45] D Böhne et al. “Status Report on the SIS/ESR Project at GSI”. In: *Proceedings of the 13th International Conference on High Energy Accelerator*. 1986, pp. 204–208.
- [46] K Blasche and B Franczak. “The heavy ion synchrotron SIS”. In: *Proc. EPAC*. Vol. 92. 1992, pp. 9–14.
- [47] J Stadlmann et al. “SIS18 operation and recent development”. In: *Proc. IPAC’23* (2023), pp. 1683–1686.

-
- [48] Bernhard Franzke. “The heavy ion storage and cooler ring project ESR at GSI”. In: *Nuclear Instruments and Methods in Physics Research Section B: Beam Interactions with Materials and Atoms* 24-25 (1987), pp. 18–25. ISSN: 0168-583X. DOI: [https://doi.org/10.1016/0168-583X\(87\)90583-0](https://doi.org/10.1016/0168-583X(87)90583-0). URL: <https://www.sciencedirect.com/science/article/pii/0168583X87905830>.
- [49] *frs manual*. URL: <https://web-docs.gsi.de/~weick/frs/frs-beamline.html>.
- [50] Helmut Weick. *Ion Optics of Fragment Separators*. Lecture at the NuSyS School, Zhuhai, China. Available via GSI lecture archive or upon request. 2024.
- [51] GSI Helmholtzzentrum für Schwerionenforschung, Darmstadt and Fair Gmbh Darmstadt. *GSI-FAIR Scientific Report 2022*. GSI Helmholtzzentrum fuer Schwerionenforschung, GSI, Darmstadt, 2023.
- [52] *FAIR*. URL: https://www.gsi.de/en/researchaccelerators/fair/the_machine.
- [53] Thomas Nilsson. “Nuclear Few-Body Physics at FAIR”. In: *Few-Body Systems* 50 (May 2011), pp. 121–127. DOI: [10.1007/s00601-010-0191-8](https://doi.org/10.1007/s00601-010-0191-8).
- [54] Hans Geissel et al. *Technical Design Report on the Super-FRS*. Darmstadt: NUSTAR, 2008, 245p. URL: <https://repository.gsi.de/record/54552>.
- [55] Stéphane Pietri et al. “Proposal to G-PAC for FAIR Phase-0: Search for new neutron-rich isotopes and exploratory studies in the element range from Terbium to Rhenium”. In: (2017).
- [56] Jan-Paul Alexander Hucka. “Control System for the Next Generation In-flight Separator Super-FRS applied for New Isotope Search with the FRS”. Dissertation. Darmstadt: Technische Universität Darmstadt, 2023. DOI: [10.26083/TUPRINTS-00023299](https://doi.org/10.26083/TUPRINTS-00023299). URL: https://tuprints.ulb.tu-darmstadt.de/view/person/Hucka=3AJan-Paul_Alexander=3A=3A.html.
- [57] Daler Amanbayev and Justus Liebig University Giessen. “Mass measurements at the N=Z and N=126 limits at the FRS Ion Catcher and development of the Cryogenic Stopping Cell for the Super-FRS”. PhD thesis. Justus-Liebig-Universität Gießen, 2023. DOI: [10.22029/JLUPUB-18567](https://doi.org/10.22029/JLUPUB-18567).
- [58] Minna Luoma. “New -decay half-lives of heavy neutron-rich nuclei and performance studies of the GEM-TPC detector”. Dissertation Draft. Jyväskylä: University of Jyväskylä, 2023.

-
- [59] Christine Hornung et al. “Mass tagging: Verification and calibration of particle identification by high-resolution mass measurements”. In: *Nuclear Instruments and Methods in Physics Research Section B: Beam Interactions with Materials and Atoms* 541 (2023), pp. 257–259. DOI: <https://doi.org/10.1016/j.nimb.2023.04.045>.
- [60] *Technical Manual Ionisation Chamber MUSIC80*. URL: https://www-windows.gsi.de/frs/technical/FRSsetup/detectors/music80/music80_manual.pdf (visited on 06/19/2025).
- [61] R. Janik et al. “Time Projection Chambers with C-pads for heavy ion tracking”. In: *Nuclear Instruments and Methods in Physics Research Section A: Accelerators, Spectrometers, Detectors and Associated Equipment* 640.1 (2011), pp. 54–57. ISSN: 0168-9002. DOI: <https://doi.org/10.1016/j.nima.2011.02.052>. URL: <https://www.sciencedirect.com/science/article/pii/S0168900211003652>.
- [62] W. R. Plaß et al. “The FRS Ion Catcher – A facility for high-precision experiments with stopped projectile and fission fragments”. In: *Nuclear Instruments and Methods in Physics Research Section B: Beam Interactions with Materials and Atoms* 317 (2013), pp. 457–462. ISSN: 0168583X. DOI: [10.1016/j.nimb.2013.07.063](https://doi.org/10.1016/j.nimb.2013.07.063).
- [63] R. Kumar et al. “Testing of a DSSSD detector for the stopped RISING project”. In: *Nuclear Instruments and Methods in Physics Research Section A: Accelerators, Spectrometers, Detectors and Associated Equipment* 598.3 (2009), pp. 754–758. ISSN: 01689002. DOI: [10.1016/j.nima.2008.08.155](https://doi.org/10.1016/j.nima.2008.08.155).
- [64] C Scheidenberger et al. “Charge states of relativistic heavy ions in matter”. In: *Nuclear Instruments and Methods in Physics Research Section B: Beam Interactions with Materials and Atoms* 142.4 (1998), pp. 441–462. ISSN: 0168-583X. DOI: [https://doi.org/10.1016/S0168-583X\(98\)00244-4](https://doi.org/10.1016/S0168-583X(98)00244-4). URL: <https://www.sciencedirect.com/science/article/pii/S0168583X98002444>.
- [65] Julien Taieb. “Etude de la production de noyaux résiduels d’évaporation issus de la réaction de spallation de l’uranium-238 par des protons à 1 GeV”. Dissertation. Orsay Cedex: Université Paris Sud, 2000. URL: <https://www.theses.fr/2000PA112294>.
- [66] O. B. Tarasov and D. Bazin. “LISE++: Exotic beam production with fragment separators and their design”. In: *Nuclear Instruments and Methods in Physics Research Section B: Beam Interactions with Materials and Atoms* 376 (2016), pp. 185–187. ISSN: 0168583X. DOI: [10.1016/j.nimb.2016.03.021](https://doi.org/10.1016/j.nimb.2016.03.021).

-
-
- [67] A. Gade et al. “One-neutron pickup into ^{49}Ca : Bound-neutron $g_{9/2}$ spectroscopic strength at $N = 29$ ”. In: *Phys. Rev. C* 93.3 (2016), 031601(R). DOI: 10.1103/PhysRevC.93.031601.
- [68] A. Kelić and et al. “Excitation of the Δ resonance in heavy-ion charge-exchange reactions”. In: *Phys. Rev. C* 70 (2004), p. 064608. DOI: 10.1103/PhysRevC.70.064608.
- [69] J. L. Rodríguez-Sánchez et al. “Study of Δ excitations in medium-mass nuclei with peripheral heavy-ion charge-exchange reactions”. In: *Phys. Lett. B* 807 (2020), p. 135565. DOI: 10.1016/j.physletb.2020.135565.
- [70] K. Haak et al. “Production and discovery of neutron-rich isotopes by fragmentation of Pt198”. In: *Physical Review C* 108.3 (2023), p. 034608. ISSN: 2469-9985. DOI: 10.1103/PhysRevC.108.034608.
- [71] O. B. Tarasov et al. “Observation of New Isotopes in the Fragmentation of 198Pt at FRIB”. In: *Physical Review Letters* 132.7 (2024), p. 072501. DOI: 10.1103/PhysRevLett.132.072501.
- [72] T. Kurtukian-Nieto et al. “Beta-decay half-lives of new neutron-rich isotopes of Re, Os and Ir approaching the r-process path near $N = 126$ ”. In: *The European Physical Journal A* 50.9 (2014). ISSN: 1434-6001. DOI: 10.1140/epja/i2014-14135-5.

Curriculum Vitae

Personal Information

Name: Heidi Ayşe Rösch-Kabadayi
Affiliation: TU Darmstadt

Education

- 2019 – 2025 Ph.D., Technische Universität Darmstadt Experimental Nuclear Physics.**
Thesis title: Search for new neutron-rich isotopes close to the N=126 magic number with the GSI Fragment Separator.
- 2017 Joint Universities Accelerator School, European Science Institute Accelerator Physics.**
- 2015 – 2019 M.Sc., Technische Universität Darmstadt Experimental Nuclear Physics.**
Thesis title: Conceptual Design of a Settings and Intensity Validation System for the Super-FRS and Preparation of Double-sided Si-Strip Detectors for FAIR-Phase-0 Experiments.
- 2009 – 2015 B.Sc., Technische Universität Darmstadt Physics.**
Thesis title: Development of a LabVIEW-based Surface with an Innovative Control for the Control System of the Spin-polarized Electron Test Source Photo-CATCH.
- 2005 – 2008 Baccalauréat Scientifique, Lycée Francais d'Ankara Charles de Gaulle.**

Publications

Kostyleva, D., Purushothaman, S., Dendooven, P., Haettner, E., Geissel, H., Ozoemelum, I., ... Rösch, H. A., ... & Scheidenberger, C. Precision of the PET activity range during irradiation with ^{10}C , ^{11}C , and ^{12}C beams. *Physics in Medicine & Biology*, (1).

Rösch, H. A., Enders, J., Espig, M., Fritzsche, Y., & Wagner, M. (2016). Development of a LabVIEW-based surface with innovative controls for the control system of the spin-polarized electron test source Photo-CATCH. *Verhandlungen der Deutschen Physikalischen Gesellschaft*.